23

Atomic and Molecular Magnets on Surfaces

Harald Brune
Institute of Condensed Matter Physics Swiss Federal Institute of Technology

Pietro Gambardella
Catalan Institute of Nanotechnology and ETH Zürich

23.1 Introduction

This chapter provides a description of atomic-scale magnets fabricated by the deposition and assembly of metal atoms and metal–organic molecules on different substrates. We describe systems composed of individual magnetic atoms, small clusters, and molecular networks as well as methods to investigate and control their magnetization, anisotropy, and temperature-dependent magnetic behavior. The experimental techniques reviewed in these pages, x-ray magnetic circular dichroism (XMCD) and scanning tunneling microscopy (STM), represent state-of-the-art probes that have a very large degree of complementarity and potential for future improvements.

Magnetic atoms on surfaces represent the ultimate limit of monodisperse magnets. Although individual atoms generally present paramagnetic behavior, their investigation provides clues to fundamental and practical issues in magnetism, such as the dependence of the magnetization on system size, atomic coordination, and composition [1]. The spin and orbital magnetic moments, exchange coupling, and magnetic ordering of such systems can be tuned by tiny changes in dimensions and coupling to the environment [2–8]. The magnetic anisotropy energy per atom can be increased by up to three orders of magnitude with respect to bulk materials, leading to metastable (blocked) magnetic states at low temperature [2,3,8]. Depending on the system size and interaction with host media, the magnetization can behave as a classical vector or be quantized, leading to effects such as magnetic hysteresis, the typical macroscale property of

a magnet, as well as quantum tunneling and phase interference effects, which are characteristic of microscopic systems [9–11]. Moreover, magnets made of one or a few atoms or molecules organized into regular patterns allow for the investigation of the ultimate limits of magnetic storage and quantum computation in novel materials [12].

23.2 Magnetic Interactions on the Atomic Scale

Regardless of the size of each system, the basic interactions that lead to magnetism are short-range, with typical lengthscales of a few Angstroms (Figure 23.1). The magnitude of the magnetization depends on the spin (m_S) and orbital (m_L) magnetic moment of each atom, as well as on the coupling between the atomic moments due to the exchange interaction, which is responsible for magnetic order. The stability of the magnetization and its preferential orientation depend on the magnetic anisotropy energy, which has two contributions: the first, called magneto-crystalline anisotropy (MCA), depends on the local environment of the magnetic ions, the second, called dipolar or shape anisotropy, depends on long-range magnetostatic interactions. Magnetic interactions in atomic-scale structures, however, can be considerably different compared to macroscopic samples. Even more importantly in some cases, interactions forbidden by symmetry in extended three-dimensional (3D) systems can suddenly become relevant [13]. Enhanced electron correlation
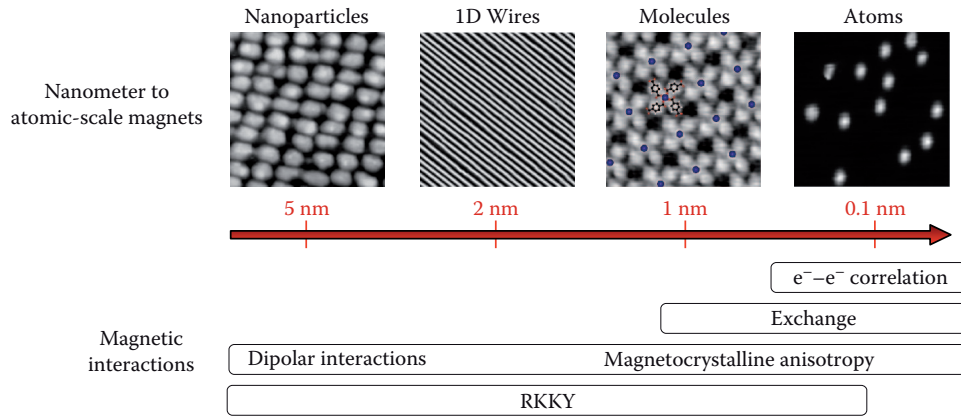
FIGURE 23.1 Schematics of magnetic structures between the nanometer and atomic scales. The numbers indicate the average dimensions of the magnetic unit cell. The range of relevant magnetic interactions is also shown.

effects in low dimensions generally lead to an increase of m_S and m_L [1], the magnetic anisotropy energy becomes a main factor determining the stability of the magnetization [3,4,14], and spin–orbit coupling (SOC) can compete with the exchange interaction and induce exotic noncollinear spin structures [15]. On nonmagnetic substrates, weak, Ruderman–Kittel–Kasuya–Yosida (RKKY) interactions mediated by conduction electrons [16–18] can induce relatively long-range coupling between small magnetic structures and significantly modify their behavior in external fields [8].

Free atoms have magnetic moments determined by the vector sum of the spin and orbital moments of electrons belonging to unfilled shells. The electron spin and orbital moment in each shell couple according to the first and second Hund's rules, respectively, which reflect the antisymmetry of the many-electron wavefunction (Pauli principle) and Coulomb repulsion effects. According to the first rule, configurations corresponding to maximum total spin (i.e., to parallel alignment of the individual spins in each shell) are favored because each electron can then occupy a different orbital state. According to the second rule, the total orbital moment is also maximized to minimize electron repulsion, compatibly with first rule. These rules allow one to predict m_S and m_L for free atoms with reasonable accuracy. The third Hund's rule determines the parallel or antiparallel alignment of m_L to m_S, depending on the sign of the SOC. In molecules and crystals, however, the atomic magnetic moments are usually strongly reduced owing to (i) the delocalization of electrons due to the overlap of the wavefunctions of neighbor atoms, which attenuates the correlation effects responsible for the first and second Hund's rule and (ii) the crystal-field potential, i.e., the electrostatic potential produced by the charges surrounding each atom, which imposes symmetry restrictions on the orbital character of the wavefunctions that influence both m_L and m_S. This is why nearly all of the transition-metal elements possess a nonzero magnetic moment as free atoms, whereas only five (Cr, Mn, Fe, Co, and Ni) retain a local moment in their bulk crystalline phases.

The appearance of magnetism in structures made by more than one magnetic atom requires the existence of local moments as a necessary condition, but also that some kind of coupling exists between them. This coupling is induced by the *interatomic* exchange interaction that arises as the wavefunction of neighboring atoms overlap and mix, leading to either ferromagnetic (FM) or antiferromagnetic (AFM) correlations between the atomic magnetic moments. Such an exchange interaction between neighboring moments is often represented, in a simplified way, by the Heisenberg model, whose Hamiltonian is

$$\mathcal{H}_{exc} = -\sum_{i,j=1}^{N} J_{i,j} \mathbf{S}_i \cdot \mathbf{S}_j. \tag{23.1}$$

In the aforementioned expression, the indices i and j run over the nearest neighbor atoms of the system ($i \neq j$), $\mathbf{S}_i$ is the spin moment of the ith atom, and $J_{i,j}$ the exchange coupling constant. As the coupling depends on the type of bond and atomic distance, $J_{i,j}$ may change from site to site. The type of coupling is determined by the sign of $J_{i,j}$, positive for FM and negative for AFM. The magnitude of J determines the robustness of magnetic order in a given system: the larger J is the stronger the tendency of the atomic moments to stay aligned to each other. Using a mean field approximation, it can be shown that the Curie temperature of an FM is given by

$$T_c = \frac{nJ(S+1)}{3k_B S}, \tag{23.2}$$

where n is the number of neighbors of each spin and k_B the Boltzmann constant. In reality, however, T_c depends not only on n but also on the dimensionality and size of the system. From a thermodynamic point of view, for example, the tendency to form magnetic ordered structures gradually decreases from 3D to two-dimensional (2D) and one-dimensional (1D) structures. Consider, for example, a 1D atomic chain consisting of N moments described by the Ising Hamiltonian $\mathcal{H}_{Ising} = -J\sum_{i=1}^{N-1} S_{zi}S_{zi+1}$ with $J > 0$, which is the uniaxial anisotropic limit of the Heisenberg model (Equation 23.1). The ground state energy of this system is $E_0 = -J(N-1)$ and

corresponds to the situation where all the moments are aligned. The lowest lying excitations are those in which a single break occurs at any one of the N sites, as shown in the following:

$$\uparrow\uparrow\uparrow\uparrow\uparrow\uparrow\uparrow\uparrow\uparrow\uparrow\uparrow\uparrow\uparrow\uparrow\uparrow \text{ ground state}$$

$$\uparrow\uparrow\uparrow\uparrow\uparrow\uparrow\uparrow\uparrow\uparrow\downarrow\downarrow\downarrow\downarrow\downarrow\downarrow \text{ lowest excited state.}$$

There are $N - 1$ such excited states, all with the same energy $E = E_0 + 2J$. At finite temperature T, the change in free energy due to these excitations is $\Delta G = 2J - k_B T \ln(N - 1)$, where the last term represents the magnetic entropy of the chain. For $N \to \infty$, we have $\Delta G < 0$ at any $T > 0$, and the FM state becomes unstable against thermal fluctuations. Only for small systems satisfying $(N - 1) < e^{2J/k_B T}$, FM order is thermodynamically stable in 1D [19].

In addition to interatomic exchange, the so-called spin Hamiltonian of a magnetic system includes single-ion terms:

$$\mathcal{H} = -\sum_{i,j=1}^{N} J_{i,j} \mathbf{S}_i \cdot \mathbf{S}_j + \sum_{i=1}^{N} h_i, \qquad (23.3)$$

where

$$h_i = -KS_z^2 - E\left(S_x^2 - S_y^2\right) - g\mu_B \mathbf{S} \cdot \mathbf{B} \qquad (23.4)$$

Here, the terms proportional to K and E represent the uniaxial and transverse magnetic anisotropy energy of the system (up to second order) and the last term the Zeeman interaction with an external magnetic field $\mathbf{B}$. The g-factor is such that $gS = m_L + m_S$. Note that, depending on the model, $\mathbf{S}$ represents either the true spin of the atom or an effective spin vector that yields the minimum multiplicity $(2S + 1)$ of the lowest lying energy states necessary to model its properties.

The MCA energy per atom is typically orders of magnitude smaller compared to the energy gained by the formation of local magnetic moments (~ 1 eV), interatomic exchange ($J_{i,j} \sim 20$ meV, $nJ \sim 200$ meV), and even minor lattice relaxations (~ 50 meV). For bulk FM, the MCA energy ranges from about 0.3 μeV/atom in fcc Ni to 2.5 μeV/atom in bcc Fe, and 45 μeV/atom in hcp-Co. Despite being so small, however, the MCA plays a fundamental role in stabilizing the magnetization with respect to external perturbations, for example, caused by temperature or external magnetic fields. This is true for macroscopic as well as for nanosized magnets. In extended systems, the large number of atoms ensures that the total MCA energy (proportional to NK) is always relatively large. In atomic-scale structures, on the other hand, NK is often comparable or even smaller than $k_B T$, meaning that thermal excitations can easily induce fluctuations of the magnetization. According to the Néel–Brown model of magnetization reversal [9], the relaxation time of the magnetization of a single-domain particle is given by an Arrhenius law of the form

$$\tau = \tau_0 \exp\left(\frac{NK}{k_B T}\right), \qquad (23.5)$$

where τ_0 is a prefactor of the order of 10^{-9} s. The energy NK can thus be considered as a barrier that hinders magnetization reversal. This barrier is extremely important for magnetic storage systems, which typically require relaxation times in excess of 10 years, i.e., $NK \gtrsim 35k_B T$. At room temperature ($k_B T \approx 25$ meV), this turns out to be a very stringent requirement for nanosized magnets, even if K can increase up to a few meV/atom in structures with low atomic coordination. Systems that behave according to Equation 23.5 are called *superparamagnetic*, because they behave similarly to a paramagnet but have a total magnetic moment that is N times that of a single atom. Such systems present magnetic hysteresis only on timescales shorter than τ. Alternatively, for a given τ, one can say that their magnetization is stable below a *blocking temperature* defined as $T_B = NK/[k_B \ln(\tau/\tau_0)]$. The miniaturization of magnetic structures thus brings new challenges for the stability of the magnetization, which must be addressed either by design or by reducing their operational temperature.

23.3 Experimental Probes

We introduce two techniques apt to the study of atomic-scale magnetic structures. Spatially averaging techniques, such as x-ray circular magnetic dichroism and x-ray linear dichroism, reveal in an element specific way the orbital and spin moments, as well as magnetic anisotropy and coupling effects. Local probe techniques, such as STM, can now access effective spin moments, magnetization curves, spin relaxation times, and exchange coupling energies atom by atom. Extended reviews of these methods can be found in References [20] and [21].

23.3.1 X-Ray Magnetic Circular Dichroism

X-ray dichroism is based on polarization-dependent x-ray absorption spectroscopy (XAS), a synchrotron radiation technique, which exploits the intense x-ray beam emitted by relativistic electrons forced to follow a curved trajectory by a bending magnet or a so-called undulator insertion device, see Figure 23.2a. In XAS, the energy of the x-rays is tuneable and the direction of the electric field vector can change from linear to right (R) or left (L) circularly polarized. The x-ray beam is monochromatized and focused before being directed onto the sample. The sample is kept in ultra-high-vacuum to avoid the absorption of x-rays from ambient gas. In a typical experiment, the x-ray energy is scanned across one or more of the absorption edges of the elements contained in the sample. As photons are absorbed, the intensity of the x-ray absorption spectra is recorded by measuring the electric current passing from ground to the sample to replace the photoemitted electrons. This method, schematized in Figure 23.2a, is called total electron yield (TEY). Other methods to measure the x-ray absorption intensity are based on the fluorescence yield or transmission yield. In the soft x-ray range used in most XMCD experiments, TEY is the most sensitive technique and, due to the limited escape depth of the electrons ($\sim$1 nm), also inherently surface sensitive.

In the simplest picture of XAS, an x-ray photon is absorbed by transferring its energy to a core electron, which is excited into an unoccupied state just above the Fermi level of the sample. TEY detects the Auger and secondary electrons that escape the sample for a core hole that decays via an Auger process. The dipole-allowed transitions of interest for magnetic studies are the core $2p \rightarrow$ valence $3d$ excitations of $3d$-transition-metal elements and the core $3d \rightarrow$ valence $4f$ transitions of the rare-earths. Figure 23.2b shows the x-ray absorption process for the spin–orbit split $2p$-core level of Co: as the x-ray energy matches the binding energy of the $2p_{3/2}$ level, an intense peak (the L_3 edge) is observed in the absorption spectrum, followed by a second one (the L_2 edge) as the x-ray energy increases up to that of the $2p_{1/2}$ level. The larger intensity of the L_3 edge compared to the L_2 edge is due to the double degeneracy of the $2p_{3/2}$ level as well as to final state effects related to SOC. A correct description of XAS beyond one-electron model requires to consider excitations from a many-electron ground state, such as $2p^6 3d^n$, to all the possible final state configurations, $2p^5 3d^{n+1}$, allowed by the dipole selection rules. In systems with localized d- or f-states, the interaction of the core hole with the valence electrons gives rise to a series of multiplets that appear as sharp features in the XAS lineshape (see Figure 23.6 for example). Such features can

be used to identify the ground state of the element under investigation using ligand field multiplet theory [22,23]. We also note that the XAS intensity depends on the symmetry and orientation of the final states relative to the x-ray polarization direction, which gives rise to *linear* dichroism effects. Here, however, we will concentrate on *circular* dichroism effects of interest for the investigation of magnetic systems.

The absorption of polarized light by a magnetized sample depends on the orientation of the magnetization **M** relative to the light polarization direction. XMCD is defined as the difference in the x-ray absorption coefficients for parallel and antiparallel orientation of the magnetization direction of the sample with respect to the helicity of circularly polarized x-rays. A qualitative understanding of XMCD can be given using a two-step model [20]. In the *first step*, R or L circularly polarized photons are absorbed and transfer their angular momentum ($\Delta m = \pm 1$, respectively) to the excited photoelectron. If the photoelectron originates from a spin–orbit split level, for example, the $p_{3/2}$ level, the angular momentum of the photon can be transferred, in part, to the spin through SOC (note: the $\Delta S = 0$ selection rule of dipole transitions holds only for ls coupling). R-polarized photons transfer opposite angular momentum to the electron than L-polarized photons, and hence one obtains large transition
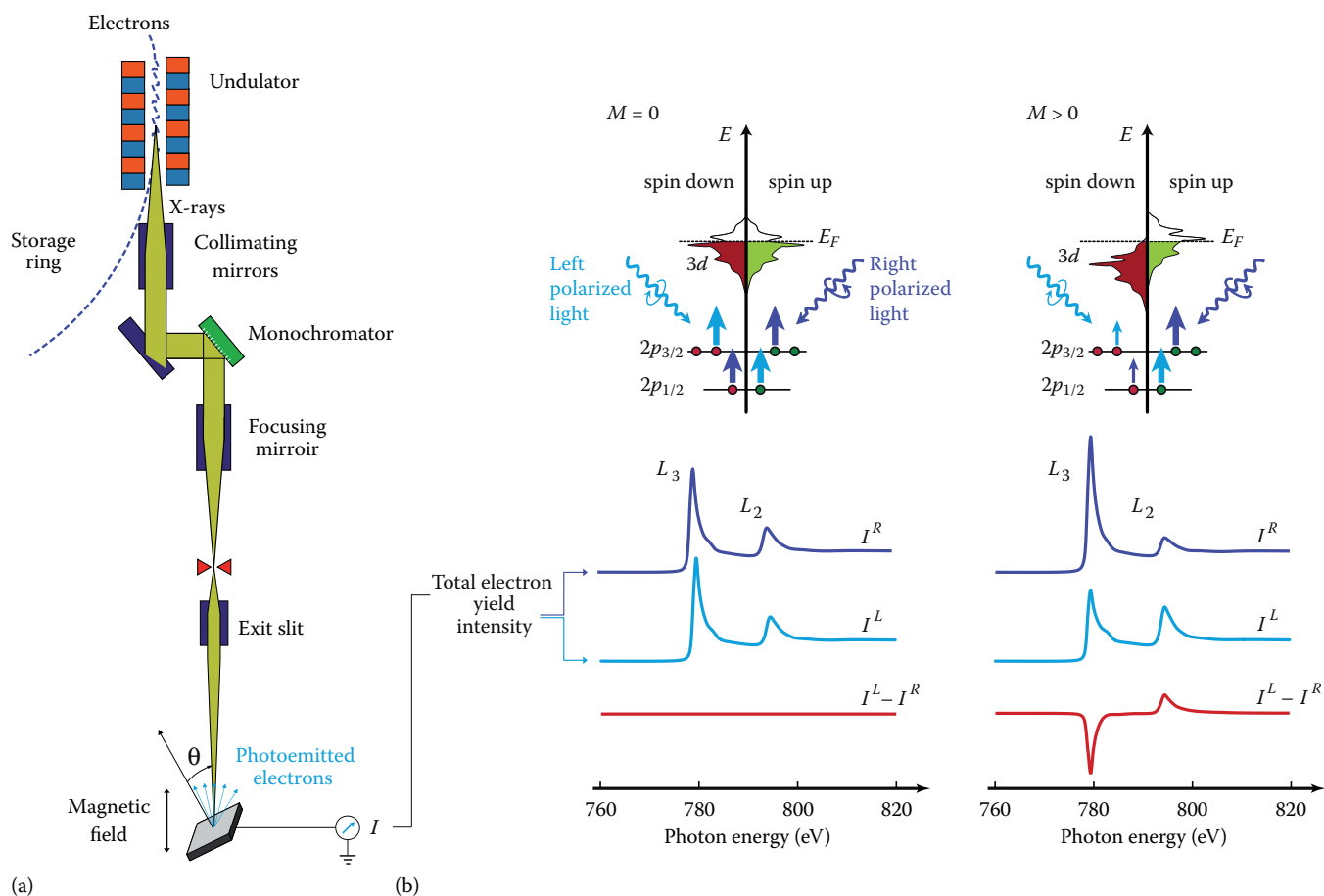

FIGURE 23.2 (a) Layout of a soft x-ray beamline. (b) Diagrams showing the excitation of $2p$ core electrons following the absorption of circularly polarized x-rays for a nonmagnetic (left) and magnetic (right) $3d$ metal. Examples of x-ray absorption spectra and XMCD are shown for the specific case of Co.

matrix elements between final states of opposite spin polarization in the two cases (see arrows in Figure 23.2b). In other words, for a given initial state, R- and L-polarized photons excite photoelectrons having opposite spin polarization. Since the $p_{3/2}$ and $p_{1/2}$ levels have opposite SOC ($l + s$ and $l - s$, respectively), the spin polarization will be opposite at the L_3 and L_2 edge.

The magnetic properties enter in the *second step*, i.e., in the promotion of the excited photoelectron to an unfilled $3d$-state of the valence band. In the absence of a net magnetization, the number of excited electrons for R or L polarization is the same for each of the L_3, L_2 edges because the total spin polarization of both the $p_{3/2}$ and $p_{1/2}$ manifolds is equal to zero. Suppose now that the $3d$ band is exchange split; the empty $3d$ states have predominantly minority character (spin up with the convention used in Figure 23.2b). The favored transitions are thus those that involve initial states with predominant minority spin. As we will show later, these are the L_3 transitions for antiparallel and the L_2 transitions for parallel direction of the magnetization with respect to the photon helicity. The exchange split final states therefore act as a filter for the spin of the excited photoelectrons. The quantization axis of the filter is that of the sample magnetization, which should be aligned with the x-ray beam direction in order to obtain the maximum XMCD intensity. We recall that the photon helicity is positive (negative) when it is parallel (antiparallel) to the light propagation direction, corresponding to R (L) polarization. The XMCD spectrum is finally obtained by taking the difference $I^L - I^R$ of two consecutive absorption spectra taken with opposite polarization. From that mentioned earlier, it follows that the XMCD intensity, normalized by the total absorption intensity $I^L + I^R$, is proportional to the inbalance between the minority and majority spins of the unoccupied states of the element under consideration, which in turn is proportional to the magnetic moment per atom.

Due to the fact that x-ray absorption is a localized process that obeys dipole selection rules, powerful sum rules exist that relate the shell-specific ground-state expectation value of m_L and m_S projected on the direction of the incident photon beam [24–26]. In the case of $2p \rightarrow 3d$ transitions, one has

$$m_L = -\frac{4}{3} \frac{\int_{L_3 + L_2} dE (I^R - I^L)}{\int_{L_3 + L_2} dE (I^R + I^L)} n_h, \qquad (23.6)$$

and

$$m_S + m_T = -\frac{6\int_{L_3} dE (I^R - I^L) - 4\int_{L_2} dE (I^R - I^L)}{3\int_{L_3 + L_2} dE (I^R + I^L)} n_h, \quad (23.7)$$

where

    E is the x-ray energy
    n_h is the number of holes in the d shell
    m_T is the intraatomic magnetic dipole moment

m_T arises from the multipole expansion of the spin density over the atomic volume and reflects the anisotropy of the spin distribution in the atomic cell. It is usually negligible in bulk samples [26], but large for single atoms [3] and molecules [27].

XMCD is thus a very powerful quantitative magnetometry tool. The XMCD intensity is element-specific and proportional to the magnetization projected on the x-ray beam direction. It is extremely sensitive [3] and, unique among magnetooptical techniques, allows for the separate measurement of m_L and m_S. Also, although not shown here, the short wavelength of x-rays offers spatial resolution down to a few tens of nm in x-ray microscopy experiments, whereas the sub-ns time structure of synchrotron x-ray beams can be exploited for ultrafast measurements [20].

23.3.2 Spin-Sensitive Scanning Tunneling Microscopy

STM has now become a mature technique for the quantitative study of the magnetism of individual atoms, molecules, and nanoscale islands adsorbed on surfaces. The first signatures of magnetism that have been detected by means of STM for individual adatoms have been midgap states for magnetic adatoms placed on a superconductor [28,29], or when superconducting tips were used for the detection of magnetism in atoms adsorbed on normal metals [1,30]. This has been closely followed by Kondo resonances in the differential conductance dI/dV [31–33] and by the suppression of one spin conductance channel for reversible STM quantum point contacts across magnetic atoms [1,30,34]. These effects reveal that the atoms possess a magnetic moment but do not determine the size of this moment and its anisotropy landscape.

Parallel to these efforts on single adatoms, spin-polarized (SP) STM has delivered valuable magnetic information on thin films and surface adsorbed nanostructures. This technique has been demonstrated for the first time on Cr(100), where an SP tip revealed the spin-contrast from terrace to terrace of this layered antiferromagnet [35]. SP-STM is now a well-established technique [21,36,37]. It has unraveled noncollinear spin ground states in thin films, which would have been difficult to guess without atomic-scale spatial magnetic resolution [15]. Furthermore, our understanding of current-induced magnetization reversal has been improved by varying the position where the SP current is injected into a nanoscale island [38], and a giant magnetoresistance of 800% has been reported [39] and explained by adsorbates in the tunnel junction [40].

Recent experiments pushed the magnetic information gained by STM significantly beyond this. As we will describe in this section, magnetization curves can now be recorded by SP-STM on single adatoms, their effective spin moments, exchange, and anisotropy energies can be deduced by spin-excitation spectroscopy (SES), and finally their spin coherence times can be determined with spin-pumping and SP-STM pump–probe experiments. Here, we describe the principles of these spin-sensitive STM measurements, while we elaborate on examples for single atoms and dimers in Section 23.4.

The magnetic contrast of SP-STM relies on the spin-valve effect, in particular, on the tunnel magnetoresistance of an STM

junction formed by a magnetic tip and a magnetic adsorbate. We explain how entire magnetization curves can be measured on isolated adatoms with this contrast. We use the example of Co/Pt(111) since for this system the first such single-atom magnetization curves have been reported [41]. In order not to be hampered by small differences in the apparent height of the adatoms, the authors used the so-called SP-STS mode, where maps of the differential conductance dI/dV, such as the ones shown in Figure 23.3a and b are recorded for given external magnetic fields. These figures show a clear spin-contrast between the two field orientations. The out-of-plane spin contrast has been achieved with Cr-coated W-tips, which were dipped into a Co ML-film on Pt(111).

dI/dV is composed of a non-polarized (np) and a polarized (pol) part, the latter being maximized for parallel and minimized for antiparallel alignment of tip and sample magnetization, thus one can write $dI/dV = dI/dV_{np} + \mathbf{M}_{tip} \cdot \mathbf{M}_{sample} \, dI/dV_{pol}$. In analogy with the polarization of the current itself, $P = (I_p - I_{ap})/$

$(I_p - I_{ap})$, where p denotes parallel and ap denotes antiparallel tip and sample magnetization, one defines a differential polarization $p = ((dI/dV)_p - (dI/dV)_{ap})/((dI/dV)_p - (dI/dV)_{ap})$.

The $M(H)$-curves shown in Figure 23.3c have been obtained by recording dI/dV images for several out-of-plane fields and laterally averaging the signal over $5 \, \text{Å} \times 5 \, \text{Å}$ squares centered at the Co atoms. As expected for magnetic tunnel junctions with soft magnetic tips, the curves have the shape of a butterfly, caused by magnetization reversal of both electrodes at different fields [41,42]. The positive field sweep (red) starts at –2 T with the magnetization of both electrodes pointing down, until at + 0.1 T one turns up reducing dI/dV, and the second electrode turns up between + 0.7 and + 1.0 T, recovering the initial dI/dV value, which stays constant up to + 2 T. The down sweep (blue) is symmetric with respect to the zero field line. From reference measurements with the same tip on a Co monolayer stripe adsorbed on the same surface, the electrode switching at ± 0.8 T is the tip. For symmetry reasons, switching of the atom takes place at exactly half way between dI/dV_p and dI/dV_{ap}, see the horizontal dash-dotted line in Figure 23.3c. The atom switches at an external field of + 0.1 T for the forward and at −0.1 T for the backward sweep. These shifts are caused by the stray field of the tip changing sign with the field sweep direction. Stray field and tip reversal have been corrected for in the curves shown in Section 23.4. SP-STM magnetization curves over individual atoms have been reported in Refs. [8,12,41,43] and over nanoscale islands in Refs. [42,44,45].

SES with the STM has recently emerged as a tool to quantify in a complementary way to $M(H)$-curves the magnetic properties of individual atoms and of very small clusters [5,46–51]. The technique relies on inelastic scanning tunneling spectroscopy measuring excitation energies with high lateral resolution and inspired by inelastic electron tunneling spectroscopy (IETS) in planar tunnel junctions [52,53]. The excitations can be vibrations [54] or changes in the magnetic state [5] of atoms or molecules in the tunnel junction, as well as surface magnons [55]. With increasing tunnel voltage, one observes a stepwise conductance increase, with a step occurring each time the tunneling electrons reach the threshold energy needed to excite a vibrational or spin degree of freedom of the system since this opens a new inelastic conductance channel. A conductance profile and the inelastic conductance channels (red arrows) are schematically represented in Figure 23.4 for the case of a $S = 5/2$ magnetic adatom prepared in the $m = +5/2$ state by a high external magnetic field pointing up. For magnetic atoms, the energies and amplitudes of the conductance steps deliver valuable information on the magnetic ground state and anisotropy of the adatoms [5,47–49], and in the case of clusters also on the Heisenberg exchange coupling between the atoms in the cluster [46,56].

Figure 23.4b shows that the symmetry of the curves about E_F bears information on the spin polarization of the tip. The tunnel current is composed of three parts, two elastic and one inelastic. The two elastic conductance channels are tunneling between tip and substrate, bypassing the magnetic atom (b_0), and tunneling into the magnetic adatom without changing its magnetic quantum state (E^- and E^+ for negative and positive tunnel voltage, V_t, respectively). The spin-polarization of the tip is schematically
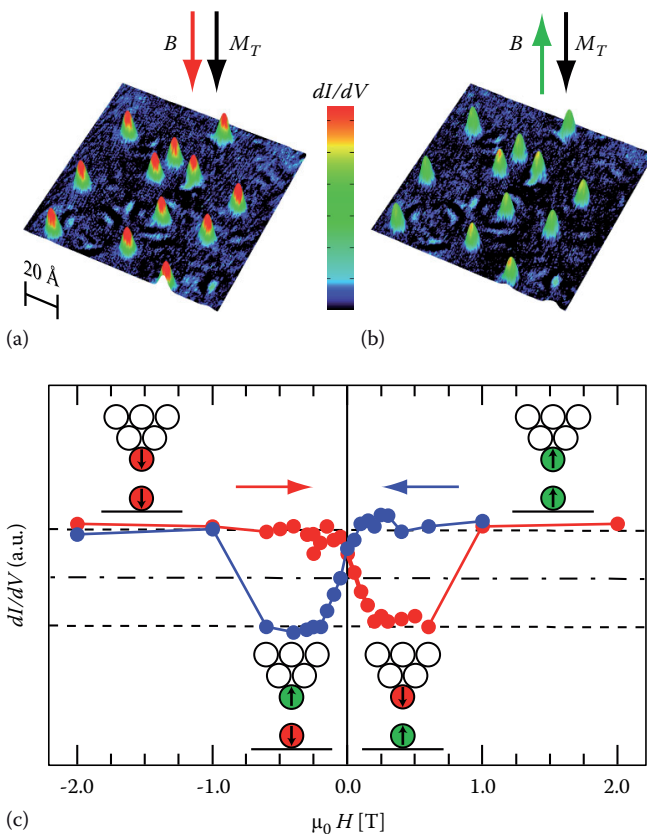

FIGURE 23.3 (a) and (b) 3D view of constant current STM images of Co atoms on Pt(111). Color code shows magnetic contrast from dI/dV for parallel (a) and antiparallel (b) field direction and tip magnetization ($V_t = 0.3$ V, $B_z = \pm 0.5$ T, and $T = 0.3$ K). (c) Magnetic-field-dependent differential conductance of soft magnetic tip over a Co atom on Pt(111). Red curves show up and blue ones down sweep of magnetic field ($I_t = 0.8$ nA, $V_t = 0.3$ V, $V_{mod} = 20$ mV, and $T = 0.3$ K). The insets indicate the relative orientation of adatom and tip **M**. The tip reverses its magnetization at around 0.8 T. The curves are shifted horizontally due to the stray field of the tip. (Adapted from Meier, F. et al., *Science*, 320, 82-86, 2008.)
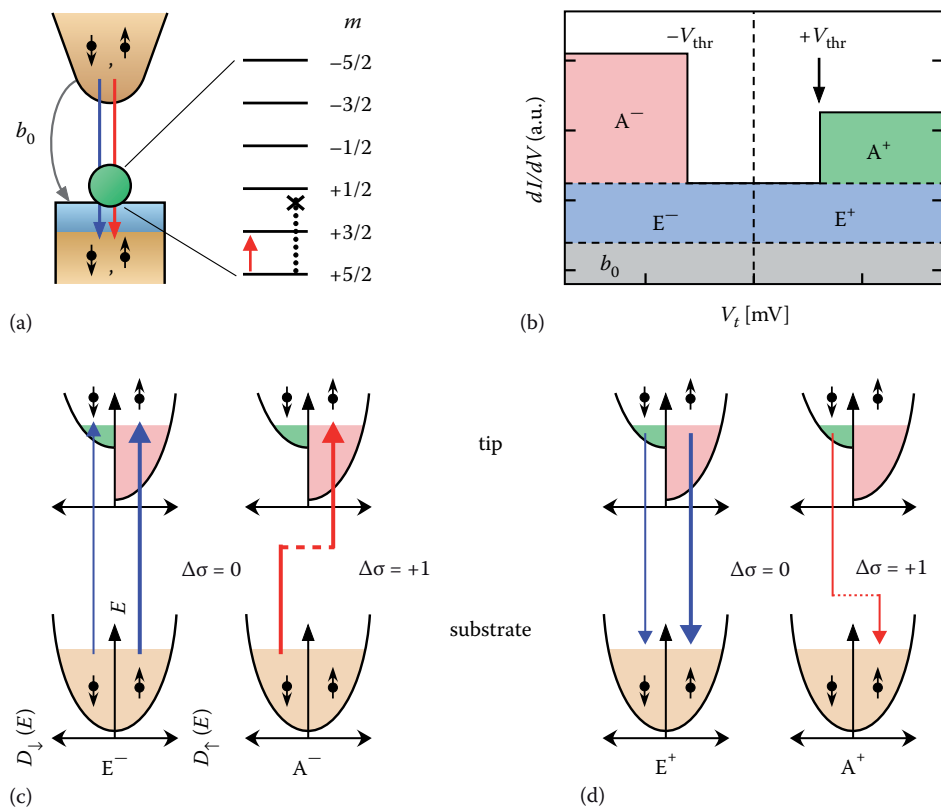
FIGURE 23.4 Spin excitation spectroscopy with a spin-polarized tip for an $S = 5/2$ magnetic impurity, such as Mn atoms adsorbed on $C_2N/Cu(100)–c(2 \times 2)$ prepared by a large out-of-plane field in the $m = +5/2$ state. (a) Schematic diagram of the possible tunnel paths when the STM tip is positioned over a Mn atom: inelastic spin-dependent tunneling (red), elastic spin-dependent tunneling (blue) and spin-independent background tunneling, b_0 (gray). Only the inelastic tunneling excites from the $m = +5/2$ to the $m = +3/2$ state. Direct excitations into higher states are forbidden (black dotted line). (b) Idealized conductance spectrum with contributions for each tunnel path: inelastic spin-dependent tunneling, A^+ (green) and A^- (red); elastic spin-dependent tunneling, E^+ and E^- (blue); spin-independent background tunneling, b_0 (gray). (c) Sketch of the tunnel paths in the spin-dependent densities of states of the STM tip (upper row) and Cu substrate (lower row) at negative voltage. The number of available states with correct spin in the tip and the substrate determines the relative strength of each tunnel path (indicated by the arrow thickness). (d) The same plot as in (c), but for positive voltage. (Adapted from Loth, S. et al., *N. J. Phys.,* 12, 125021, 2010.)

shown in the density of states plots with spin-down electrons and spin-up electrons. If the magnetic state is unchanged (black arrows), tunneling takes place between identical spin states of both electrodes ($\Delta\sigma = 0$), and even though there is a higher current for the majority spin, the total current does not depend on the sign of the bias voltage (V_t). This is different for the third conductance channel where the tunnel electrons undergo a spin-flip, $\Delta\sigma = \pm1$. For a Mn atom prepared in the $m = +5/2$ state, the only change can be $\Delta m = -1$, therefore the electrons can make a spin-flip only from spin down to spin up ($\Delta\sigma = 1$). For negative polarity, the final state of this inelastic channel is a majority state, while for positive polarity the initial state is a minority state leading to the shown asymmetry for energies above and below E_F [57,58].

As will be shown later, this spin-polarization can be used to progressively excite the magnetic system in the tunnel junction, which is referred to as spin-pumping. The decay of the *dI/dV* signal for energies beyond the threshold for SES and as function of tunnel current gives access to the life-time of the excited states [58]. As we will show in the following section, this spin-relaxation time can also be accessed by a SP-STM pump–probe experiment

where a pump voltage pulse excites the system and a probe pulse measures its magnetic state a delay time after the probe [59].

These examples illustrate how the initial satisfaction to detect some signature of magnetism with the STM has now been replaced by the capacity of pinning down magnitudes of magnetic moments, anisotropy energies, magnetic ground and excited state configurations, entire magnetization curves, and spin relaxation times. This evolution of STM as a sensor of atomic magnetism is moving on rapidly and is expected to have strong impact on our understanding of quantum magnetism, magnetic impurities in solids, and magnetism of entities composed of a few atoms or molecules only.

23.4 Magnetism of Single Atoms and Clusters on Surfaces

Although most transition-metal atoms possess a magnetic moment in the gas-phase, the survival of this moment when an atom is placed on a nonmagnetic substrate is not granted. Owing to their reduced atomic coordination, surface adatoms can be viewed as a bridge

between the atomic and solid state, with many of their electronic and magnetic properties determined by the competition between the Coulomb energy and the kinetic energy associated with electrons hopping from site to site in the lattice [60]. For moderate hybridization between adatom and host electron states, the Anderson model [61] describes well the formation of a magnetic moment. Many-body spin-flip processes may also lead to the Kondo effect, the screening of the local moment by conduction electron spins, which can be directly visualized by scanning tunneling spectroscopy [31,33].

From a different perspective, controlling the bonding, diffusion, and nucleation processes of adatoms at surfaces offers countless opportunities to tune the adatom–substrate interaction as well as to construct multiatom magnetic clusters of tailored shape and dimensions [62]. Adatoms and clusters may further be considered as the precursors of thin films, as the growth of magnetic mono- and multilayers is typically initiated by the deposition of transition-metal atoms from the vapor phase onto a nonmagnetic substrate. Investigating substrate–impurity hybridization and coordination effects thus provides basic understanding and useful guidelines to tailor the magnetization and magnetic anisotropy of nanomagnets and optimize sensitive interface properties that govern the performances of magnetic storage media and electron transport in spintronic devices. In the perspective of this book, adatoms and clusters on nonmagnetic surfaces represent the ultimate paradigm of atomic-scale magnets, whose behavior can approach that of classical or quantum magnets depending on the adatom–substrate and adatom–adatom interactions.

23.4.1 Hybridization with the Substrate

The first effect noticed when a transition-metal atom is deposited on a metallic substrate is a reduction of m_S and m_L compared to the free atom case. Figure 23.5 shows a set of density functional calculations of the atomic moment of $3d$, $4d$, and $5d$ adatoms adsorbed on the (100) face of an Ag substrate [63–65]. The adatoms still follow the Hund's first rule with maximal moments at the center of each series; however, their magnetic moment assumes smaller, noninteger values relative to the gas phase. For example, a Co free atom with seven electrons in the d-shell has $m_S = 3$ and $m_L = 3$ μ_B, which reduce to about $m_S = 2$ and $m_L = 1$ μ_B on Pt(111) [2] and Ag(100) [65] owing to charge transfer from the substrate into the Co $3d$-states and hybridization. The larger relative decrease of m_L compared to m_S is related to the hierarchy of the Hund's rules, as electron delocalization reduces Coulomb repulsion effects within the d-states. Note that the local moment tends to decrease further with increasing atomic coordination, as shown by the calculations performed for monolayer films. Interestingly, elements that are nonmagnetic in the bulk display sizeable magnetic moments as adatoms, including $4d$ and $5d$ elements. This allows for a much broader choice of elements in the construction of atomic-scale magnets. The reduction of the magnetic moments due to the increase of hybridization with coordination number is greater for $5d$ and $4d$ elements because of the larger extension of their wavefunctions compared to $3d$ metals. As a rule of thumb, it can be shown that the atomic magnetic moment decreases with increasing atomic coordination proportionally to the inverse of the width of the d-band [66].

XMCD [1,3] and photoemission [60] studies show that the degree of hybridization of the $3d$-states of single adatoms depends very significantly on the electron density of the substrate, even for simple sp metals like the alkalis. However, even for very small mixing between the $3d$-states and substrate conduction electron bands, charge transfer can occur and affect the magnitude of m_S and m_L. This is nicely seen by analyzing the multiplet features of the x-ray absorption spectra of Co adatoms
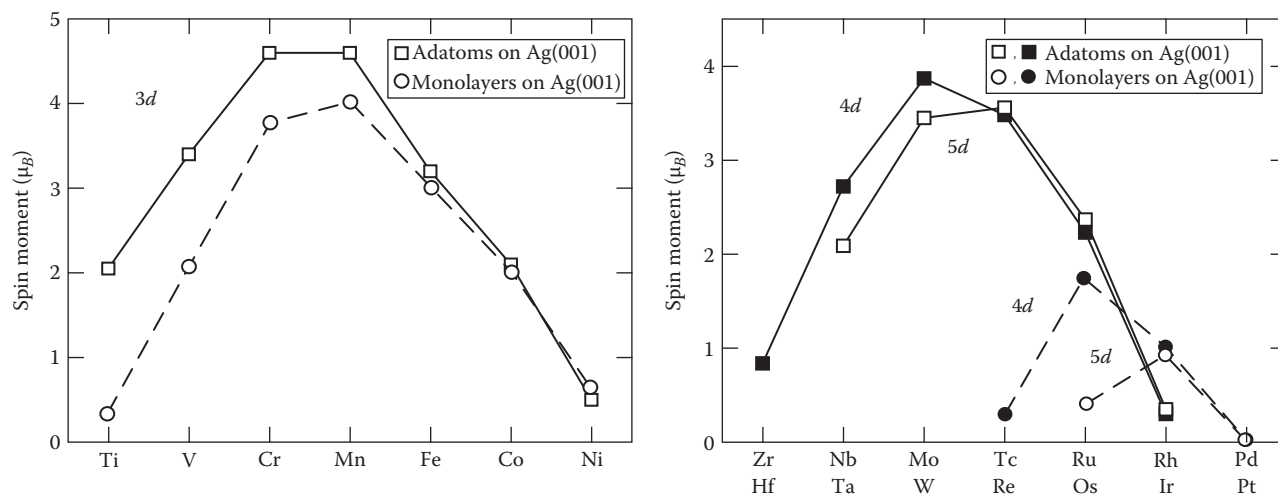

FIGURE 23.5 Spin magnetic moments calculated for (a) $3d$ and (b) $4d$ and $5d$ transition metal adatoms at the hollowsite of Ag(100) (squares connected by full lines) and monolayers on Ag(100) (circles connected by dashed lines). (Adapted from Blügel, S., *Phys. Rev. Lett.*, 68, 851, 1992; Lang, P. et al., *Solid State Commun.*, 92, 755, 1994; Nonas, B. et al., *Phys. Rev. Lett.*, 86, 2146, 2001; Blügel, S., Magnetism goes nano: 36th IFF Spring School, In: S. Blügel, T. Brückel, C. M. Schneider eds., Ch. *Reduced Dimensions I: Magnetic Moment and Magnetic Structure*, Forschungszentrums Jülich, Jülich, 2005. With permission from the authors.)
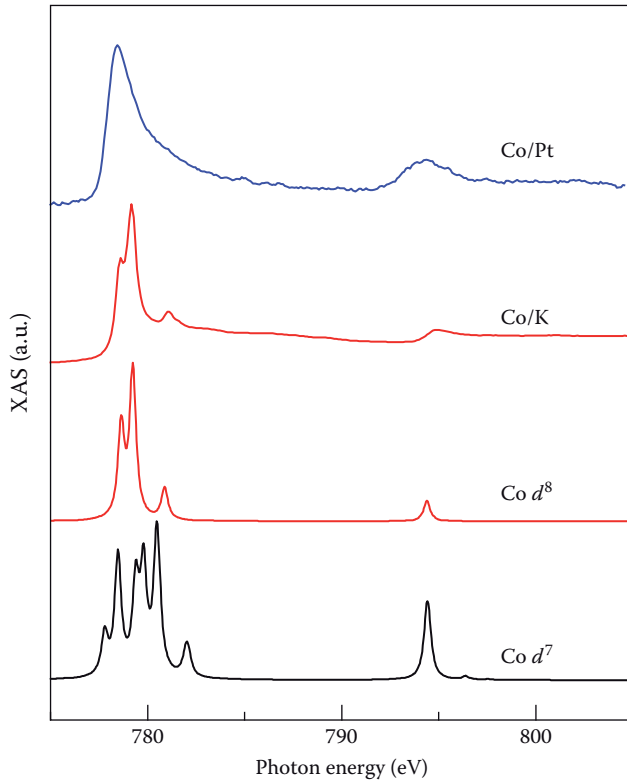
FIGURE 23.6 Experimental and theoretical x-ray absorption spectra of Co impurities in the $L_{3,2}$ edge region. The experimental spectra were recorded as the sum of the absorption intensity in total electron yield for parallel (I^R) and antiparallel (I^L) alignment of the photon helicity with respect to the magnetic field $B = 7$ T at an angle $\theta = 0°$ relative to the surface normal. The temperature of the Pt(111) and K substrates was 6 K and 10 K, respectively. The theoretical spectra were calculated using an atomic multiplet model [23] for d^7 and d^8 configurations. (Adapted from Gambardella, P. et al., *Phys. Rev. Lett.*, 88, 047202, 2002.)

on a K surface, as shown in Figure 23.6. The narrow XAS multiplet structure observed for Co_1/K indicates that the Co ground state has a strongly localized character, specifically a $3d^8$ configuration with nearly atomic-like $m_S \approx 2$ and $m_L \approx 3\ \mu_B$ [3]. Note that the spectra expected for the d^7 and d^8 ground states of free Co atoms are very different, indicating that the occupation of the Co $3d$-states increases by one electron upon deposition on K. The hybridization of the Co d-states changes drastically from being very weak for Cs to much stronger for Li along the alkali group, as the electronic density of alkali metals increases for the lighter species. Transition-metal substrates differ from free-electron like metal surfaces not only due to their larger conduction electron density but also for the presence of unfilled d-states crossing the Fermi level, which heavily affect most of their magnetic properties (e.g., the susceptibility and magnetoresistance) as well as the nonmagnetic ones (e.g., cohesion, diffusion barriers, catalytic activity, etc.). As an example of a strongly interacting substrate, we present data for isolated Co adatoms on the (111) surface of Pt [2]. The x-ray absorption spectra of Co_1/Pt(111) are much broader and present no clear multiplet feature compared to those of Co_1/K (Figure 23.6) as the adatom $3d$-states hybridize

strongly with both the $5d$- and $6s$-states of the substrate. This is accompanied by a substantial decrease of m_L to about 1.1 μ_B, whereas m_S remains close to 2 μ_B.

23.4.2 Magnetization Curves for Ensembles vs. Individual Atoms

Given the pronounced anisotropic spatial extension of the d-orbitals, the Co–Pt admixture of $3d$- and $5d$-states may lead to unequal filling of electronic states with different symmetry, and hence to a strong anisotropy of the orbital magnetization. Due to the strong SOC between m_S and m_L, a strong magnetic anisotropy of the overall magnetization is to be expected. Figure 23.7a shows the intensity of the XMCD Co L_3 minimum measured for **B** and x-ray beam oriented out-of-plane (black) and at 70° with respect to the surface normal (red). In order to account for the dependence of the cross section with angle, the signal has been normalized by the XAS intensity. It is seen that the magnitude of the saturation signal differs by more than 60% for the two field directions, revealing the presence of extraordinary magnetic anisotropy.

The fixed-energy L_3 intensity depends on the linear combination $m_S + 3m_L + m_T$, Equations 23.6 and 23.7, but it can be demonstrated that the three moments m_S, m_L, and m_T follow the same field dependence, i.e., that the XMCD L_3 signal is proportional to the total Co magnetic moment projected onto the beam, respectively, field direction. Therefore, the curves shown in Figure 23.7a are XMCD magnetization curves that can be fitted in the framework of a classical model, where the time-averaged projection of the total impurity moment $\langle m \rangle$ on the magnetic field direction is given by

$$\langle m \rangle = m_0 \frac{\int \widehat{\mathbf{m}} \cdot \widehat{\mathbf{B}} \exp[(\mathbf{m} \cdot \mathbf{B} + K(\widehat{\mathbf{m}} \cdot \widehat{\mathbf{e}})^2)/k_B T] d\Omega}{\int \exp[(\mathbf{m} \cdot \mathbf{B} + K(\widehat{\mathbf{m}} \cdot \widehat{\mathbf{e}})^2)/k_B T] d\Omega}. \tag{23.8}$$

Here, m_0 stands for the saturation value of the Co plus induced Pt moment, $\widehat{\mathbf{e}}$, $\widehat{\mathbf{m}}$, and $\widehat{\mathbf{B}}$ represent the unit vectors of the easy axis, the magnetic moment, and the field direction, respectively; K is a uniaxial magnetic anisotropy barrier, and the integration is carried out over the solid angle Ω of the magnetic moment in spherical coordinates. The solid lines represent fits of the data by means of numerical integration of Equation 23.8 with m and K as free parameters fitted simultaneously for the two curves.

Note that, in such a model, all directions are in principle allowed for the Co magnetic moment, showing that a classical description is well-suited to describe a strongly hybridized impurity system. Moreover, owing to the strong Stoner enhancement factor of Pt, the substrate atoms are highly polarized by $3d$ transition-metal species, developing a significant intrinsic magnetization that decays exponentially away from the impurity site. In dilute bulk CoPt alloys with 1% at Co concentration, the total moment per Co atom is of the order of 10 μ_B [67]. In our case of surface dilute impurities, the fit of Equation 23.8 yields $m = 5.0 \pm 0.6\ \mu_B$ and $K = 9.3 \pm 1.6$ meV.
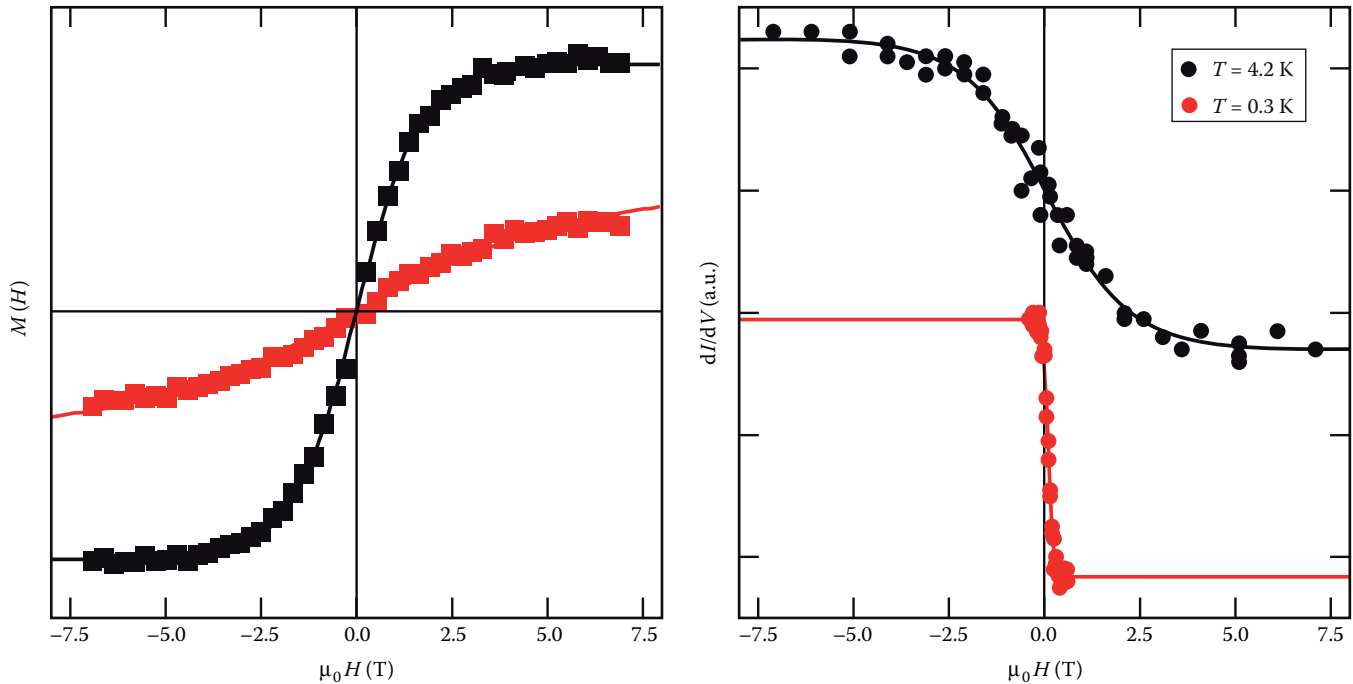
FIGURE 23.7 Comparison of magnetization curves of ensembles of adatoms measured with XMCD and of an individual adatom measured with SP-STM, both for Co/Pt(111). (a) Field dependence of the Co L_3-XMCD signal normalized to the total XAS intensity. The out-of-plane projection of the magnetization is shown in black, the one where B and x-ray beam are at 70° with respect to the surface normal in red (Θ = 0.03 ML, T_{dep} = 5.5 K, and T_{XMCD} = 5.5 K). (Adapted from Gambardella, P. et al., *Science*, 300, 1130, 2003.) (b) $M(H)$-curves on an individual atom at T = 4.2 K (black) and 0.3 K (red) (I_t = 0.8 nA, V_t = 0.3 V, and V_{mod} = 20 mV). (Adapted from Meier, F. et al., *Science*, 320, 82–86, 2008.) Symbols in (a) and (b) represent experimental data, solid lines are fits according to the functions described in the text.

These values remain unchanged on samples with Co coverage comprised between 0.007 ML and 0.03 ML, showing that magnetic or electronic interactions between the adatoms are negligible. We note that weak inelastic features at energies close to the expected 9 meV have been reported in dI/dV spectra recorded above Co adatoms on Pt(111) at high tunnel current [49]. These features have been assigned to spin excitations; however, an unequivocal proof would require to study their magnetic field dependence, which is hampered by their large energetic width.

$M(H)$-curves measured by SP-STM for the same system using the method described in Section 23.3.2 are shown in Figure 23.7b. STM can measure such curves over individual atoms and therefore report on variations associated by the atomic environment of the respective atom. It cannot measure the angular dependence of the magnetization, but $M(H)$ curves at different temperatures over the very same Co atom, as shown for 4.2 (black) and 0.3 K (red). The absence of hysteresis down to 0.3 K is not expected for an uniaxial MCA energy barrier of the order of 10 meV. $M(H,T)$ fits were performed using a simple Hamiltonian $\mathcal{H} = -m(B - B_{tip})\cos(\theta) - K\cos^2(\theta)$, where B_{tip} is the stray field from the tip and θ the angle between the magnetic moment m and the sample normal. The fit parameters are m, the saturation value of the spin-dependent dI/dV contrast M_{sat}, and B_{tip}; K = 9.3 meV was taken according to the XMCD measurements presented earlier. SP-STM on about 80 different Co atoms evidenced narrow m-distributions at 4.2 K with a mean value

of 3.7 μ_B. This is lower than the total moment detected in XMCD, but consistent with the sum of the Co spin and orbital moment, meaning that SP-STM is sensitive to this sum but not to the moments induced in the Pt substrate. However, the moment distribution obtained for the different atoms at 0.3 K is rather broad ($2\,\mu_B \leq m \leq 6\,\mu_B$). This has been attributed to substrate-mediated RKKY interactions with a coupling energy ranging from about 10 to 180 μeV [41,43]. At 4 K, these interactions are smaller than thermal excitations and at 0.3 K they become apparent.

These results show that single Co atoms on Pt(111) behave as paramagnetic impurities when placed in an STM junction biased at 0.3 V. This voltage has been chosen in order to obtain comparable magnetic contrast for Co atoms adsorbed on the two non-equivalent threefold Pt(111) hollow sites [41,68]. The absence of remanence might therefore well be due to spin excitations induced by the tunnel electrons. The atoms are subject to substrate-mediated RKKY interactions, which can be detected down to 10 μeV resolution by recording the exchange field stemming from a FM monolayer high stripe attached to a substrate step. Once single magnetic atoms are subject to such interactions, remanence becomes apparent in SP-STM also with electron energies beyond the threshold for spin-excitations [12].

A second source for the absence of remanence can be quantum tunneling of the magnetization. The likelihood of this process depends on the amplitude of the anisotropy energy variation in a plane perpendicular to the designated magnetization axis.
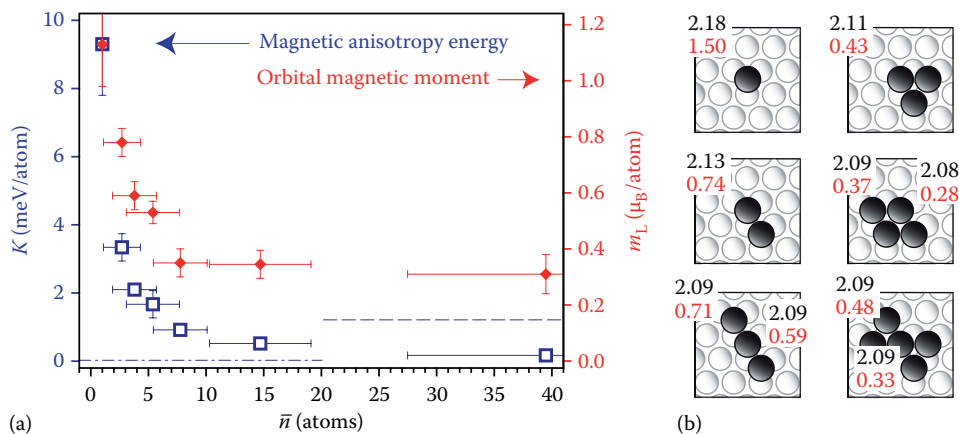
FIGURE 23.8 (a) Orbital moment m_L (red diamonds) and anisotropy energy K (blue open squares) as a function of the average cluster size $\bar{n}$ for $Co_n/Pt(111)$. For comparison, the blue dashed and dashed-dotted lines show the MCA energy per Co atom of the $L1_0$ CoPt alloy and hcp-Co, respectively. The error bars on the horizontal scale represent the standard deviation of the size distribution determined by STM. (b) m_s (black) and m_L (red) calculated using density functional theory for the differently coordinated atoms en the $Co_n/Pt(111)$ clusters. (Adapted from Gambardella, P. et al., S*cience*, 300, 1130, 2003.)

The present case of Co/Pt(111) has sixfold transverse symmetry implying higher order terms in the transverse anisotropy and thus the matrix element for magnetization reversal by tunneling is expected to be small. Therefore, XMCD measurements at $T < 2$ K, or SP-STM $M(H)$ curves recorded at $V_t < 10$ meV, might well reveal remanence for a single atom for this system.

XMCD experiments and ab initio calculations also show that m_L and the MCA of small Co_N clusters are dramatically sensitive to unit changes of the atomic coordination [2,14], as shown in Figure 23.8. This tendency, governed by lateral adatom–adatom interactions as well as substrate–adatom interactions, continues from adatoms to clusters and thin films until eventually the bulk values of $m_L = 0.15$ μ_B and $m_S = 1.6$ μ_B are reached.

23.4.3 Magnetic Anisotropy from STM Spin Excitation Spectroscopy

The first STM recorded differential conductance steps stemming from spin excitations were reported for Mn atoms adsorbed on an oxide monolayer on a metal surface [5]. This layer has been the self-limiting $Al_{10}O_{13}$ layer formed by exposing a NiAl(110) surface at high temperature to oxygen [69]. The conductance steps appeared only in the presence of an external magnetic field. Due to the small excitation energies involved, the measurements had to be performed at 0.6 K. The step energies were proportional to the magnetic field, $E_{step} = g\mu_B B$, yielding the Landé g-value for Mn atoms as a function of their adsorption site. The results were with $g = 1.88 \pm 0.02$ for Mn on the oxide and 2.01 ± 0.03 for Mn at the edge of the oxide close to the free electron value of 2.0023. The amplitudes of the conductance steps were with 20%–60% significant and very sensitive to the atomic environment. Mn atoms adsorbed directly onto NiAl(110) did not show the steps. Therefore, the insulating layer enhances the cross section for spin scattering. However, STM-SES also works for magnetic adatoms directly adsorbed onto a metal surface. Inelastic conductance steps with a height of 5%

and the magnetic field shift identifying them as magnetic excitations have been reported for Fe/Cu(111) [51].

We outline how quantitative information on the anisotropy landscape and effective spin moments can be gained from SES taking different transition metal atoms on copper-nitride monolayer patches on a copper (100) surface as example [47,48]. Figure 23.9a shows an STM image of square Cu_2 N-islands with a $c(2 \times 2)$ structure separated by clean Cu bands appearing as narrow vertical and wider horizontal ridges. The island pattern is typical for chemisorbed N on Cu(100) [70]. The island size is determined by an optimum between strain and edge energy, and their equidistant arrangement is established by long-range elastic interactions mediated by the substrate [71]. Note that the islands are not exactly forming a $c(2 \times 2)$ structure, STM measurements reveal that the Cu_2N lattice constant is slightly larger than $\sqrt{2}\,d_{nn, Cu}$ [72]. Density functional theory (DFT) calculations show that the N atoms are almost at the same height as the first atomic Cu plane [47]. One therefore speaks of a Cu_2 N-layer rather than of a N/Cu(100) adlayer. The adsorbates visible as protrusions are adsorbed Mn, Fe, and Co atoms.

Spectra taken on Mn show clear (10%–20%) conductance steps at very low energies. As determined from assembling atomic chains of these atoms with AFM order [46], Mn has a spin of $S = 5/2$, as in the gas phase. The fact that there is a conductance step at zero field, together with the fact that it shifts in the presence of a magnetic field, signifies that the atoms have a magnetocrystalline anisotropy energy. SES for different field directions can be analyzed in terms of the anisotropy energy landscape by using the spin-Hamiltonian, which we give here in the nomenclature introduced for molecular magnets:

$$H = g\mu_B \mathbf{B}\cdot\mathbf{S} + D\hat{S}_z^{\,2} + E\left(\hat{S}_x^{\,2} - \hat{S}_y^{\,2}\right). \qquad (23.9)$$

The first term is the Zeeman energy, and the following two represent the axial and transverse anisotropies D and E, respectively. The assignment of the axes is such as to maximize $|D|$
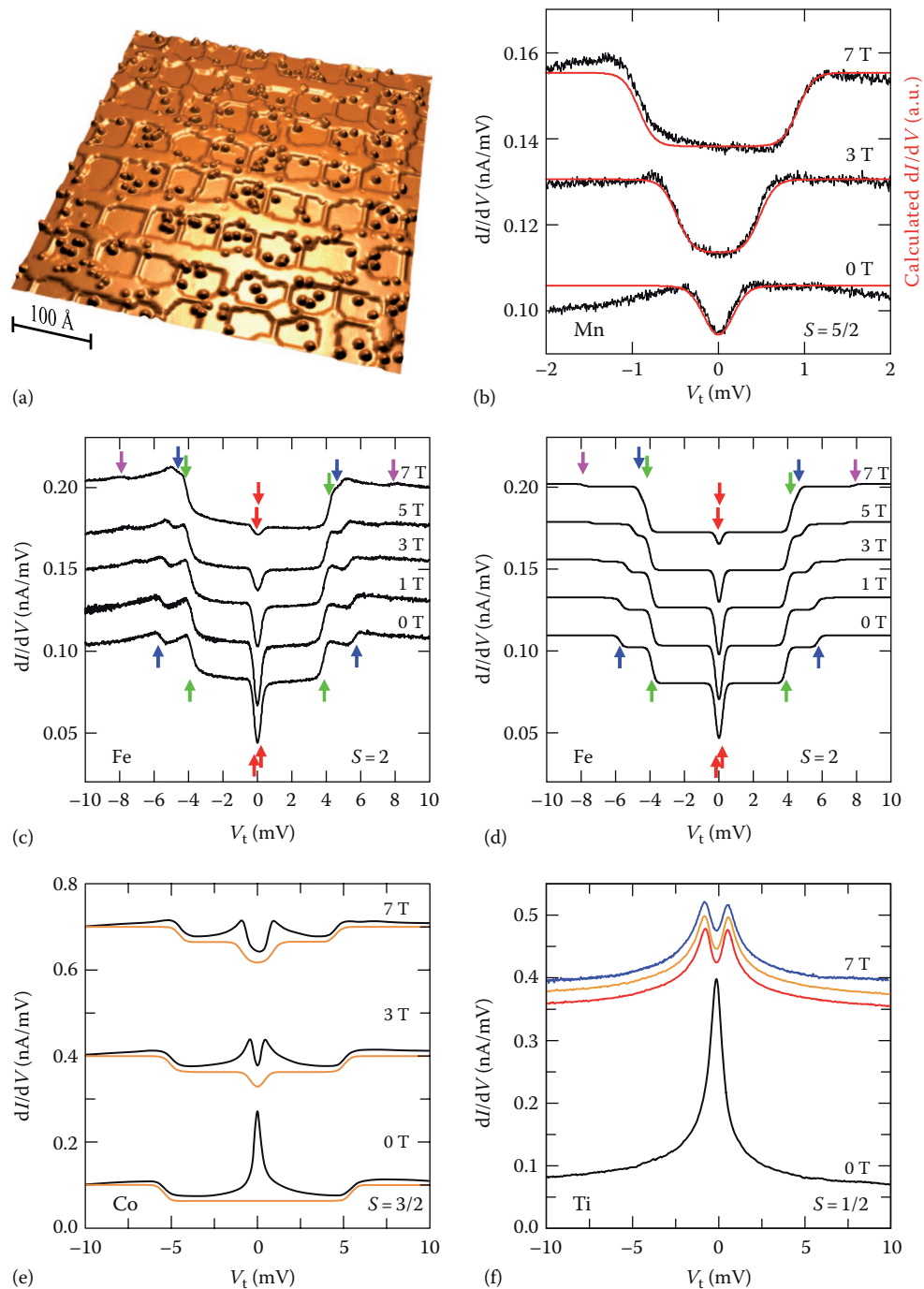
FIGURE 23.9 (a) Constant current STM image showing square Cu_2N-patches on Cu(100) appearing lower than the clean Cu ridges. The adatoms are Mn, Fe, and Co (500 Å × 500 Å, $V_t = 10$ mV, $I_t = 0.5$ nA, and $T = 5$ K). (b) Field-dependent dI/dV over Mn together with calculated spin-excitation spectrum in red. (c) Spectra over Fe. (d) Calculated SES. (e) Spectra over Co together with calculated SES in yellow (for (b), (c), and (e) tip stabilized at $V_t = 10$ mV, $I_t = 1.0$ nA, $V_{mod, rms} = 20$ μV, $f_{mod} = 800$ Hz, and $T = 0.5$ K). (f) dI/dV for Ti showing the Kondo resonance and its isotropic splitting for magnetic field along three orthogonal directions (red and yellow in-plane, blue out-of-plane, $V_{mod, rms} = 50$ μV, $f_{mod} = 745$ Hz, and $T = 0.5$ K). The lower curves give absolute dI/dV, the upper ones have been offset for clarity. (Adapted from Otte, A.F. et al., *Nat. Phys.*, 4, 847, 2008; Hirjibehedin, C.F. et al., *Science*, 317, 1199–1203, 2007.)

and to yield $E > 0$. By diagonalization of Equation 23.9, one finds the eigenvectors Ψ_i and calculates the spin excitation spectrum considering the selection rule that initial and final state are connected by $\Delta m = \pm 1$ given by the spin-flip of the tunnel electrons. The resulting red curves in Figure 23.9b fit very well the energies and step heights for the shown out-of-plane field direction. Fitting these curves for all three orthogonal field directions and using $S = 5/2$ reveals that Mn adsorbed onto a Cu site on $Cu_2N/Cu(100) - c(2 \times 2)$ has out-of-plane easy axis anisotropy with $D = -0.039 \pm 0.001$ meV, a very small transverse term of $E = 0.007 \pm 0.001$ meV, and a Landé factor of $g = 1.90 \pm 0.01$.

One can reproduce the essential features neglecting E. This simplifies the picture as then the eigenstates are pure $m = -5/2$, $-3/2$, $-1/2$, $+1/2$, $+3/2$, and $+5/2$, with m being the z-projection of the magnetization. For $B = 0$, there are three sets of doubly degenerate energy levels. From low to high energy these are $m = \pm 5/2$, $\pm 3/2$, and $\pm 1/2$. At $T = 0.5$ K, the thermal population of the higher energy levels can be ignored. The step seen at 0 T therefore corresponds to the two transitions $m = \pm 5/2 \rightarrow \pm 3/2$. Their energy difference is $D((5/2)^2 - (3/2)^2) = 0.16$ meV in agreement with the observed excitation energy. For large B, all of the levels are non-degenerate and the levels are separated by much more than the thermal energy. Therefore, only the $-5/2$ ground state is populated and the step seen in the upper two curves marks the excitation from this state to $m = -3/2$. Transitions to higher lying levels are forbidden by conservation of the total angular momentum. The outward shift of the conductance steps with out-of-plane field is due to the field stabilizing the ground state. The expected shift is the Zeeman energy for $\Delta S = 1$ being 0.77 meV for a field of 7 T, thus positioning the step at 0.93 meV, again in agreement with observation.

Figure 23.9c shows the spin excitation spectrum for an Fe atom on an identical adsorption site as Mn. The zero field spectrum shows three with respect to E_F symmetric pairs of conductance steps located at 0.2, 3.8, and 5.7 meV. Applying a magnetic field along the in-plane direction where the Fe atom has no nearest N neighbors, the so-called hollow direction, some steps move and some out. Under the assumption that $S = 2$, all step positions and step heights for all field values and directions could perfectly be fitted by $g = 2.11 \pm 0.05$, $D = -1.55 \pm 0.01$ meV, $E = 0.32 \pm 0.01$ meV, and with z along the in-plane direction where the Fe atom has N atoms as nearest neighbors. The agreement with the calculated curves shown in Figure 23.9d is striking. Note that there is a fourth peak expected from the calculations (purple arrow), which can also be guessed from the 7 T spectrum. In order to compare D with the uniaxial anisotropy K, used in bulk, thin films and nanostructures and referred to in Section 23.3.1, one has to multiply D by S^2 and thus obtain anisotropies almost as large as the ones of Co/Pt(111) [2]. Easy axis anisotropy implies that the zero field ground state has large and identical weights in the $m = \pm 2$ eigenstates with very little weight also in $m = 0$ since the finite transverse E-term mixes states of different m. This gives rise to more than one excitation step. DFT calculations confirm the choice of $S = 2$ but also show that Fe pushes the underlying Cu atom deep below the first atomic plane and

therefore forms an adsorption complex with the neighboring N atoms and the underlying Cu, having similarities with the configuration in molecular magnets [47].

The zero field spectrum of Co reproduced in Figure 23.9e exhibits conductance steps around ± 6 meV, together with a prominent Kondo peak centered at E_F [48]. Analysis of the field-dependent step energies, identical to the one described earlier for Mn and Fe, leads to $S = 3/2$, $D = 2.75 \pm 0.05$ meV, and $g = 2.19 \pm 0.09$. The positive D-term signifies easy plane anisotropy. Therefore, the lowest energy states have small projection onto the designated z-axis, and the magnetic ground state is a twofold degenerate $m = \pm 1/2$ doublet. This is the necessary condition for the Kondo effect of a high-spin impurity as these two states are linked by $\Delta m = \pm 1$, enabling Kondo scattering of the conduction electrons. Mn and Fe are high-spin impurities with easy axis anisotropy and therefore the lowest energy states are separated by $\Delta m > 1$, excluding first-order Kondo scattering and naturally explaining the absence of a Kondo feature for these adsorbates. These low-T STM observations highlight the role of magnetic anisotropy in the Kondo effect for high-spin impurities.

The last example is a Ti atom having $S = 1/2$. The spectrum of Figure 23.9f shows a large Kondo peak with isotropic field splitting, but no indication of spin-excitation steps. Ti is adsorbed on the same site than the other transition metal atoms; thus, it is subject to the same crystal field that obviously induces no magnetocrystalline anisotropy in a low-spin impurity. We close this part on SES of single adatoms with the remark that the anisotropy deduced from the conductance steps for Fe/Cu(111) is in perfect agreement with the one inferred from single atom SP-STM magnetization curves [51].

We now turn to ensembles containing a few magnetic atoms and illustrate how textbook examples of low-dimensional magnetism, such as Heisenberg chains, can be assembled and studied by means of STM. Vertical atom transfer [73,74] was used to assemble straight Mn_n chains with the STM, again on $Cu_2N/Cu(100)$. The chains displayed a striking parity dependence on their SES. Chains with even number of atoms n had no conductance step close to 0 eV, but large steps at several meV energy, while chains with odd n displayed zero-energy steps together with less pronounced ones at higher energy. The absence of low energy spin excitation in even chains implies a ground state with $S = 0$ and their presence in odd chains an $S \neq 0$ ground state. Therefore, the chains were AFM and hence a realization of Heisenberg chains with finite length [75]. The dimer conductance steps split up into three in an external magnetic field. Accordingly, they were attributed to transitions from the $S_{tot} = 0$ singlet to the $S_{tot} = 1$ triplet state with magnetic quantum numbers $m = 0$, ± 1. The step positions were used to derive the exchange energy $J = 6.2$ meV from a Heisenberg Hamiltonian. The spin per Mn atom could be inferred to $S = 5/2$ from the position of the IETS step of Mn_3. Note that $S = 5/2$ is also the spin of a free Mn atom. From the known J and S values, the spin transitions for all chain lengths can be derived from a Heisenberg open-chain model, and the values were in excellent agreement with experiment for chain length up to six atoms. The most recent

example of small clusters with AFM order are chains of Fe atoms on the same substrate that represent the smallest reported AFM with stable magnetization state [56]. Note that SES-STM has also been used to explore the magnetic anisotropy in surface adsorbed metal–organic molecules [76,77] and to probe super-exchange interaction in molecular magnets [78].

23.4.4 STM Spin Pumping

We illustrate in this section how STM can be used to manipulate the magnetic quantum state and access the spin relaxation times of individual atoms or molecules adsorbed onto surfaces. Successive tunnel electrons injected from a SP tip at time intervals smaller than the spin-relaxation time can pump the magnetic system through the momentum transfer during the course of inelastic spin excitations into higher excited states. This can best be observed if the magnetic system is prepared by an external magnetic field in a ground state from which excitation can only be done with one sign of Δm such that a suitable SP tip leads to a net excitation only for one sign of the tunnel voltage. The average time between successive electrons determines how

many excitations are possible before relaxation and therefore the non-equilibrium spin-population. For high tunnel currents, this can lead to the inversion of the spin population compared with the one favored by the external field. The SP conductance through the magnetic impurity depends on its magnetic quantum state and therefore allows this state to be read out. Note that this dependence is not the regular SP-STM contrast described by the SP-local density of states of tip and sample, but it is due to SP tunnel electrons that interact with m but do not change it. The excitation and the simultaneous read-out of the magnetic state lead to a strong current dependence of the dI/dV signal that can be used to infer the spin-relaxation time τ_1 of excited states [58].

As schematically outlined in Figure 23.4 and explained in the corresponding section earlier, SP-STM tips give rise to asymmetric spin-excitation step heights in dI/dV. Figure 23.10a shows such asymmetries for SES recorded with a SP tip over Mn atoms adsorbed on Cu_2N, whereas these asymmetries are absent for a non-SP tip as seen in Figure 23.10b. The SP tip has been created by picking up a Mn atom from the surface to the tip apex, and the non-SP tip by dropping it off and picking up a Cu atom. Since Mn has a very weak out-of-plane anisotropy and $S = 5/2$,
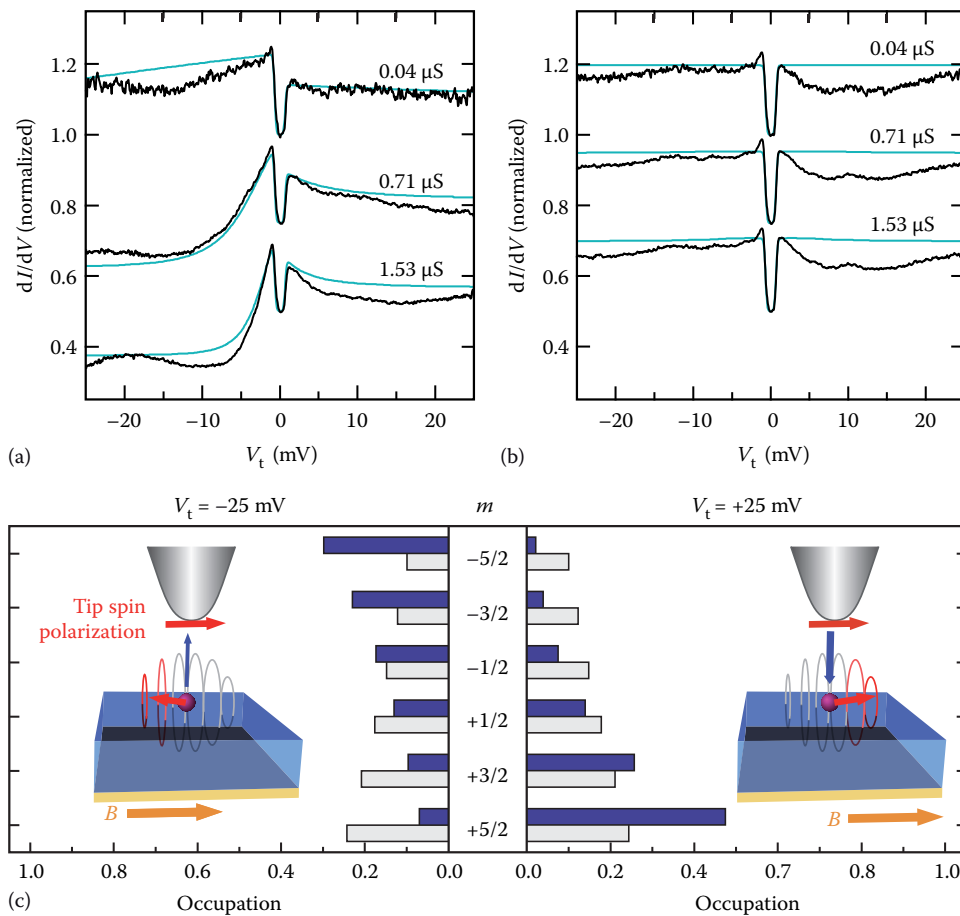

FIGURE 23.10 Spin-pumping for $Mn/Cu_2N/Cu(100)$-$c(2 \times 2)$. Tunnel spectra over the same Mn atom, (a) recorded with a spin-polarized and (b) with a non-spin-polarized tip (black measured, turquoise calculated spectra, $B = 7$ T in-plane, $T = 0.5$ K, dI/dV normalized to 1 at $V_t = 0$ V, spectra offset by –0.3 for clarity). The spectra are labeled by σ_0, the value of the conductance at $V_t = 0$. (c) Populations of magnetic quantum states for positive and negative tunnel bias and for SP (blue) and non-SP (gray) STM tip. (Adapted from Loth, S. et al., *Nat. Phys.*, 6, 340, 2010.)

application of a small magnetic field in any direction prepares it in the $m = +5/2$ state. The tip atom is a paramagnetic impurity with low anisotropy that saturates at 1 T at 0.5 K, thus fields beyond this value fully magnetize tip and Mn atom alike. For negative polarity, the majority electrons can excite the Mn atom to the $m = +3/2$ state, while for positive polarity of the tunnel junction, this excitation can only be done by minority electrons. This difference results in the different inelastic conduction step heights in Figure 23.10a, which can directly be read out in terms of the spin-polarization of the tip, yielding $\eta = 0.24 \pm 0.04$ in (a) and evidently $\eta = 0$ in (b).

The negative polarity side of the spectra recorded with the SP tip levels off very strongly for high tunnel conductance, ($\sigma_0 \geq 0.71\ \mu S$), reaching an asymptotic value already at $V_t = -10$ mV. This signifies that the Mn atom has a spin-population with large weight in the $m = -5/2$ state, where the magnetization points opposite to the field. For that state, the elastic conductance is 0.99 spin sensitive, explaining the large drop of the overall conductance. Note that also the conductance on the positive polarity side changes slightly with increasing tunnel current, being due to spin-excitations by tip minority electrons. Figure 23.10c shows the spin population for the SP (dark gray bars) and the non-SP tip (light gray bars) for both junction polarities. Note that, in the present case, all excitations have the same energy, therefore the different m states form a spin ladder with equidistant states and all excitations appear at a single energy. This is different for a Mn dimer that has been used to distinguish the different excitations [58].

Fits of the I_t decay at $V_t < -V_{exc}$ give lifetimes τ_1 of the first excited state, i.e., for $m = 3/2 \rightarrow m = 5/2$, of $\tau_1 = 0.25 \pm 0.04$ ns

at 7 T and $\tau_1 = 0.73 \pm 0.10$ ns at 3 T. The spin relaxation takes place by interaction with substrate conduction electrons. Their number is proportional to the energy of the inelastic excitation, which is by Zeeman energy proportional to the magnetic field. To first order, the spin relaxation time τ_1 is therefore expected to be inversely proportional to B, which is indeed what is found. Spin-phonon coupling plays no significant role as decay mechanism of the magnetic state.

Another example of the manipulation of the magnetic quantum state of an adatom with a magnetic STM tip has been through exchange interaction between adatom and tip [79]. Note also a theory paper discussing the spin torque induced change of magnetization of adatom [80], which has experimentally been realized and discussed earlier for Mn/Cu$_2$N.

23.4.5 Magnetic Relaxation Times from STM Pump–Probe Experiments

The time resolution of STM is limited by the bandwidth of current-to-voltage amplifier used to measure the tunnel current. This bandwidth is sufficient to resolve the flicker noise caused by thermal magnetization reversal of magnetic islands in SP-STM [38,81,82]. However, it is orders of magnitude slower than the relaxation times of magnetic quantum states of individual atoms and molecules. As sketched in Figure 23.11a, it suffices to use a high bandpass electronics for the tunnel voltage [59]. As discussed earlier, a magnetic system saturated by an external field can be excited to higher lying states by injection of SP electrons with energy beyond the threshold for spin excitations, eV_{thr}.
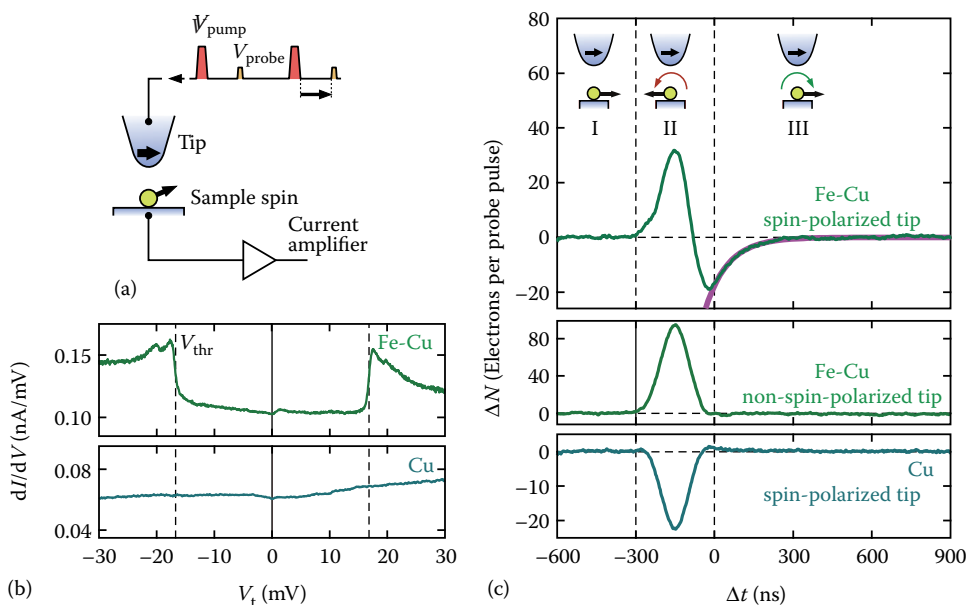

FIGURE 23.11 STM pump–probe experiments on an FeCu dimer on Cu$_2$N/Cu(100)–$c(2 \times 2)$. (a) Sketch of the sequence of tunnel voltage pulses, the delay time Δt is from the end of the pump to the beginning of the probe pulse, as indicated by the arrow. (b) SES steps at ± 16.7 mV in dI/dV over the dimer, whereas the reference spectrum over Cu adatom shows no inelastic features, both spectra have been recorded with a non-polarized tip. (c) $\Delta N(\Delta t) := N(\Delta t) - N(-600$ ns$)$ for spin-polarized tip above FeCu dimer (upper panel), with a non-polarized tip above the FeCu dimer (middle), and with a spin-polarized tip above the Cu atom (lower panel) ($V_{pulse} = 36.5$ mV, FWHM = 100 ns, rise and fall times 50 ns, $V_{probe} = -4.0$ mV). (b) and (c) $B = 7$ T out-of-plane and $T = 0.6$ K. (Adapted from Loth, S. et al., *Science*, 329, 1628, 2010.)

These electrons may stem from a paramagnetic tip that is saturated by the same external field. A pump pulse with $V_t > V_{thr}$ excites the system and a probe pulse with $V_t < V_{thr}$ follows after a delay time to read out the magnetic state by its m-dependent conductance. Inside the tunnel, voltage is zero such that the magnetic state outside the pulses does not contribute to the tunnel current. The DC tunnel current averaged over many pump–probe sequences depends on the delay time since the mean conductance depends on whether the magnetic system is still in its excited state when the probe pulse comes, or whether it has had time to decay into the ground state.

This method has been demonstrated on an FeCu dimer on $Cu_2N/Cu(100)$-$c(2 \times 2)$ [59]. This dimer has $S = 2$ and easy axis magnetic anisotropy as single Fe atoms on this surface; however, the dimer anisotropy is close to out-of-plane instead of in-plane, and D is of much larger magnitude. The latter causes the first spin excitation energy to be at much higher tunnel voltage, as seen from the inelastic conductance steps in Figure 23.11b $V_{thr} = 16.7$ mV. Figure 23.11c shows the difference $\Delta N(\Delta t)$ between the number of electrons detected per probe pulse for a given delay time $N(\Delta t)$ and this number for a delay time of $\Delta t = -600$ ns, i.e., for a probe pulse preceding the pump pulse. The upper panel shows this quantity for an SP tip above the dimer. In region I $\Delta N(\Delta t) = 0$ since the dimer is in its ground state, the pump pulse influences the system long after the probe pulse. In region II, there is a large positive peak for -300 ns $\leq \Delta t \geq -100$ ns, followed by a strong decrease in the conductance. The positive peak is caused by the overlap of pump and probe pulse, their sum is applied to the tunnel junction. The conductance decrease is caused by the magnetization of the dimer pointing opposite to the one of the tip during the probe pulse and therefore the tunnel-magnetoresistance of the junction is high. For positive delay times, the conductance recovers exponentially with a time constant of $\tau_1 = 87 \pm 1$ ns, as deduced from the fit of ΔN in region III of Figure 23.11c. This is the dimers spin-relaxation time at $T = 0.6$ K and $B = 7$ T in-plane field.

The reference measurements shown in the lower two panels of Figure 23.11c demonstrate that the exponential decay for $\Delta t \geq 0$ is only obtained for a SP tip above a magnetic impurity. An identical pump–probe sequence applied with a non-polarized tip above the dimer gives only the positive Gaussian peak but no sign change and exponential decay since the tunnel junction is insensitive to the orientation of the dimer magnetization. The $\Delta N(\Delta t)$-curve obtained with an SP-tip above a Cu atom shows a dip as a sign of the cross-correlation between pump and probe pulse. When both pulses overlap, $|V_t|$ is higher and the associated I_t change depends on d^2I/dV^2, which seems to have opposite signs for FeCu and Cu at the relevant energy. The authors ensured that the STM observation does not influence the dimer's relaxation time. τ_1 is independent of V_{pump}, as long as $|V_{pump}| \geq |V_{thr}|$; it is further independent of the pump pulse length and tip-sample distance. Both polarities of V_{pump} work; however, negative polarity works better due to spin momentum transfer from the tip, increasing the spin excitation cross section.

The state from which the dimer decays within τ_1 is the $m = -2$ state. This can be explained as follows. The highest energy excitation is from the ground state $m = +2$ to $m = +1$ requiring 16.7 meV. Since all other excitations require less energy, all states, including $m = 0$, are accessible once $|V_{pump}| \geq |V_{thr}|$. The rate-limiting step in the de-excitation is the one with the highest barrier, i.e., $m = -2 \rightarrow +2$. The relaxation mechanism is likely magnetic tunneling and not thermally assisted due to the absence of a T-dependence of τ_1 for 1 K $\leq T <$ 10 K at $B = 5.5$ T. Only from 10 K onward, one sees evidence for the decrease of τ_1, which can be due to onset of thermal reversal. The B-dependence of τ_1 is an increase up to 6 T and a decrease beyond this value. The first is due to the reduced tunnel matrix element by increased Zeeman splitting of the $m = \pm 2$ states and the second by transverse field component mixing of states.

Altogether, these measurements of single adatoms and of very small clusters, being them taken out by means of XMCD for mono-disperse ensembles or on individual objects by means of STM, show that an increase by one to two orders of magnitude in magnetic anisotropy energy with respect to bulk or 2D films can be obtained by reducing the size of magnetic particles to a few tens of atoms or less on suitable substrates. This is very beneficial to increase the stability of the magnetic moment, according to Equation 23.5. However, while this holds for a single atom, it is obvious that the overall stability of the magnetization of an N-atom cluster is governed by the sum over the MCA energy contributions from each atom. As more atoms are assembled together to fabricate clusters with a large total magnetic moment and a total MCA strong enough to stabilize FM behavior against thermal fluctuations, this gain is countered by the decrease of the MCA per atom with increasing size (Figure 23.8a). The problem, however, can be circumvented by noting that the atomic coordination rather than the absolute particle size is the key parameter that governs the magnitude of the MCA, m_L, and m_S, see, e.g., Figure 23.8b). Surface supported atomic-scale structures where the shape and composition are tuned so as to control the coordination of the magnetic atoms and maximize useful interface effects, such as in core-shell 2D particles [83], 1D atomic wires [4,84], 2D metal–organic networks [85], and single molecules [6,86,87], offer very interesting opportunities to exploit such effects. Examples for the latter two are discussed in the next section.

23.5 Magnetism of Molecular Networks and Single Molecules on Surfaces

Individual atoms are difficult to arrange in thermally robust regular patterns on surfaces. Moreover, their magnetic properties are dominated by the type of substrate because of electronic hybridization. These problems can be overcome by embedding the magnetic atoms into a planar molecular framework [85]. However, whereas the chemistry of metal–organic complexes is well established, little is known about the electronic and magnetic properties of atomically thin metal–organic grids interfaced with a metallic substrate or electrode. We analyze here two approaches

to this problem, one relying on the supramolecular synthesis of 2D metal–organic networks on appropriate surfaces and the other on the deposition of integral molecules such as metal phthalocyanines [7,27,88,89] and single molecule magnets (SMMs) [6].

23.5.1 Self-Assembled Supramolecular Spin Networks

The codeposition of transition metal ions and organic ligands on crystalline surfaces offers the potential to design supramolecular grids with programmable structural and chemical features, where the interaction with the substrate is used to stabilize a planar geometry [90,91]. For example, Fe atoms coadsorbed with terephthalic acid (TPA) molecules on Cu(100) in ultrahigh-vacuum constitute a prototypical 2D hetero-assembled system forming a variety of mono- and bi-nuclear network structures, whose morphology is determined by the Fe:TPA stoichiometry, substrate symmetry, and annealing temperature [90]. Figure 23.12a shows a hard sphere model of a square planar $Fe(TPA)_4$ network obtained by sequential deposition of TPA and Fe on Cu(100), where each Fe atom is coordinated to four

TPA molecules through Fe-carboxylate bonds, with the supramolecular $Fe(TPA)_4$ units organized in a (6×6) unit cell with respect to the underlying Cu lattice [85]. Weak hydrogen bonding interactions between the complexes favor long-range order extending over entire terraces of the substrate. The resulting superlattice of individual Fe atoms has perfect 15×15 Å periodicity (Figure 23.12b). XAS shows that the $3d$-states of the Fe ions in the molecular network are highly localized compared to single Fe adatoms adsorbed on Cu(100), and have an almost pure d^6 character (Fe^{2+}), with maximum 14% d^7 weight [85]. These results indicate that coordination bonds have formed between the Fe centers and carboxylate ligands, with partial decoupling of Fe from the metal substrate. Such bonds, which involve Fe $3d$ and O $2p$ states, explain the fourfold coordination geometry as well as the thermal stability of these complexes. XAS also proves that the $Fe(TPA)_4$ network is formed by high-spin Fe^{2+} ions, which is interesting because Fe^{2+} is expected to favor large MCA (i.e., zero field splitting) and anisotropic g-factors. Indeed, contrary to Fe atoms on Cu(100) that have very small MCA, XMCD measurements of $Fe(TPA)_4$ show a very strong anisotropic magnetization with in-plane easy axis (Figure 23.12c).
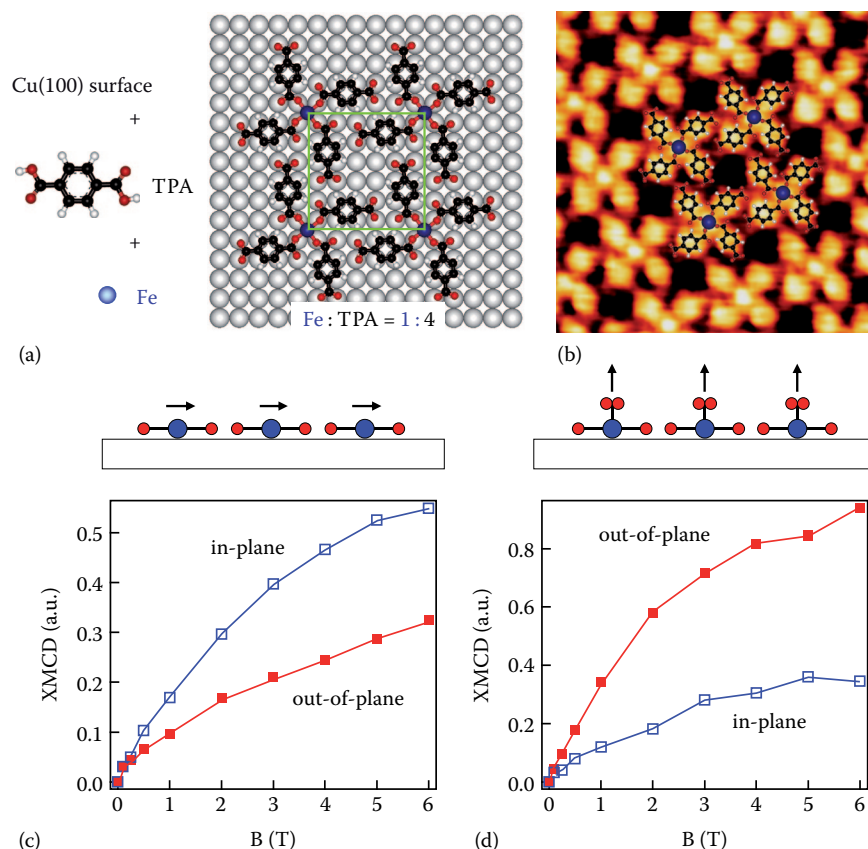

FIGURE 23.12 Planar supramolecular networks of $Fe(TPA)_4$ complexes self-assembled on Cu(100). (a) Ball and stick model and (b) STM image of the $Fe(TPA)_4$ array. Blue dots indicate the position of Fe atoms, red O, black C, white H. (c) Element-selective magnetization curves of the Fe centers of $Fe(TPA)_4$ and (d) O_2-$Fe(TPA)_4$ measured by XMCD at $T = 8$ K with magnetic field applied out-of-plane ($\theta = 0°$, red full symbols) and close to the in-plane direction ($\theta = 70°$, blue open symbols). The data points represent the Fe XMCD intensity integrated over the L_3 edge and normalized by the corresponding L_3 integrated XAS intensity. The diagrams show the easy axis magnetization direction. (Adapted from Gambardella, P. et al., *Nat. Mater.*, 8, 189, 2009.)

Such networks are of interest not only as a way to organize individual spins in a regular pattern but also because of the possibility to tune their magnetic susceptibility by chemical means. The coordination of the metal ions with lateral molecular ligands yields stable but unsaturated coordination bonds, which allow for the chemical modification of the electronic and magnetic properties of the magnetic atoms independently from the substrate. This was shown by exposing an $Fe(TPA)_4$ network to O_2, which binds as an axial ligand on top of the active Fe sites [85]. A prolonged exposure to O_2 results in a saturated O_2-$Fe(TPA)_4$ network that has distinct properties with respect to $Fe(TPA)_4$. Although the formal Fe oxidation state remains 2^+, the symmetry of the ligand field acting on Fe changes from square-planar in $Fe(TPA)_4$ to pyramidal in O_2-$Fe(TPA)_4$ and electron localization effects increase gradually with the number of ligands, favoring electronic decoupling of the Fe atoms from the substrate. Density functional calculations show that the formation of the supramolecular complexes is accompanied by a substantial increase of the Fe-substrate distance, calculated as 2.32 Å for individual Fe atoms on Cu(100), 2.71 Å for $Fe(TPA)_4$, and 3.32 Å for O_2-$Fe(TPA)_4$ [85]. XMCD reveals the presence of large local magnetic moments on Fe, and in particular of increasing orbital moments going from Fe_1/Cu(100) (0.18 ± 0.03 μ_B), to $Fe(TPA)_4$ (0.42 ± 0.06 μ_B), and to O_2-$Fe(TPA)_4$ (0.55 ± 0.07 μ_B), measured at 8 K parallel to the easy magnetization direction. Most importantly, angle-dependent XMCD measurements show that O_2 adsorption at the Fe sites drives an abrupt spin reorientation transition, rotating the Fe easy axis out-of-plane (Figure 23.12d). This easy axis switch can be explained as the axial ligand induces a change of the Fe ground state from A_{1g} to E_g in O_2-$Fe(TPA)_4$, as expected based on symmetry arguments. The E_g term is an orbitally degenerate doublet with nonzero m_L pointing along the principal symmetry direction, which explains the tendency of O_2-$Fe(TPA)_4$ to magnetize out-of-plane, together with its enhanced orbital moment compared to $Fe(TPA)_4$.

Controlling the magnetic anisotropy of spin networks independently from the substrate is a key issue in the development of molecule–metal interfaces for spintronic applications, both at the level of single molecules and extended layers. With respect to bulk molecular crystals, the planar and open coordination structure of 2D supramolecular array make such systems extremely sensitive to ligand modifications, providing a handle to the spin orientation and enhanced chemical sensitivity of the magnetization. The capability to fabricate 2D arrays of monodisperse spin centers with nanometer spacing, and to understand and control their magnetic properties at the interface with a metal substrate, constitutes a basic step toward the exploitation of single spin phenomena in small scale devices.

23.5.2 Arrays of Metal Phthalocyanines

A different strategy to isolate and arrange single spins on surfaces is to directly sublimate magnetic molecules by means of thermal evaporation in vacuum. This works particularly well for small and compact molecules, which are usually chemically stable and can withstand temperatures of the order of a few hundreds of degrees C. Metal phthalocyanines (MPc) constitute a model system for investigating the properties of magnetic molecules on surfaces using this approach [7,27,88,89,92,93]. MPc are well-known metal–organic complexes with applications in organic electronics and photovoltaics. They are formed by a central metal ion (M) coordinated by an aromatic macrocyclic ligand (Pc), as shown in Figure 23.13a. More than 70 metal ions have been found to be able to coordinate to the Pc ligand, giving rise to a broad variety of chemical, electronic, and magnetic properties. When deposited on metal surfaces, MPc adopt a flat adsorption geometry placing both the M and Pc species in contact with the substrate. Moreover, van der Waals molecular interactions and spontaneous registry with the substrate lead to the self-assembly of ordered monolayers [77], as shown in Figure 23.13b for CuPc on Ag(100). The lattice spacing of a monolayer of MPc is about 15 Å, similar to that of $Fe(TPA)_4$.

As for single metal atoms, the first question to address in this case is if and how much of the pristine MPc magnetic moment survives adsorption on a substrate. There is no unique answer to this point, depending on the type of substrate as well as on the symmetry of the unoccupied d-states of the M ions [27,88,89,93]. It is generally believed that charge transfer from the substrate to metal d-states extending perpendicularly to the Pc plane leads to total or partial quench of the molecular magnetic moment. However, this is but a partial picture of the interaction between surface and molecules. We present here a case study of CuPc deposited on Ag(100) to highlight some additional aspects. According to XMCD measurements, CuPc complexes forming a compact molecular layer on Ag(100) conserve their gas-phase magnetic moment, $m_S = 1$ and $m_L = 0.1$ μ_B, corresponding to a Cu^{2+} ion with a $b_{1g}(d_{x^2-y^2})$ ground state, $S = 1/2$, and small SOC-induced orbital moment [27]. This agrees with the weak Cu-Ag hybridization expected for the $d_{x^2-y^2}$ orbital of Cu due to its planar symmetry. However, STM measurements reveal a delocalized Kondo resonance on isolated CuPc molecules (Figure 23.14), evidencing the presence of an additional spin on CuPc induced by charge transfer from Ag to the $2e_g$ orbital of the Pc ligand (the gas-phase lowest unoccupied molecular orbital of CuPc) [7]. Thus, the magnetic moment of single CuPc molecules increases rather than decrease after adsorption, leading to a triplet ground state with $S = S_M + S_{Pc} = 1$ (Figure 23.14a). A similar phenomenon occurs on NiPc, which is diamagnetic in the gas phase, leading to $S = S_{Pc} = 1/2$ [7].

STM also offers the possibility to manipulate individual molecules with atomic-scale precision (Figure 23.14b). Molecular structures of arbitrary shape and size can be assembled in this way, such as the 3×3 "molecular sudoku" (shown in Figure 23.14c). Besides playing LEGO with molecules, such an approach is useful to study the effect of lateral interactions between molecules on their electronic structure. The spectroscopy maps reported in Figure 23.14d reveal that the Kondo resonance (−6 meV) due to the unpaired spin found in the $2e_g$ Pc orbital disappears in molecules with more than two nearest neighbors due to the gradual upshift of the $2e_g$ state from about −0.3 eV in single CuPc (not shown)
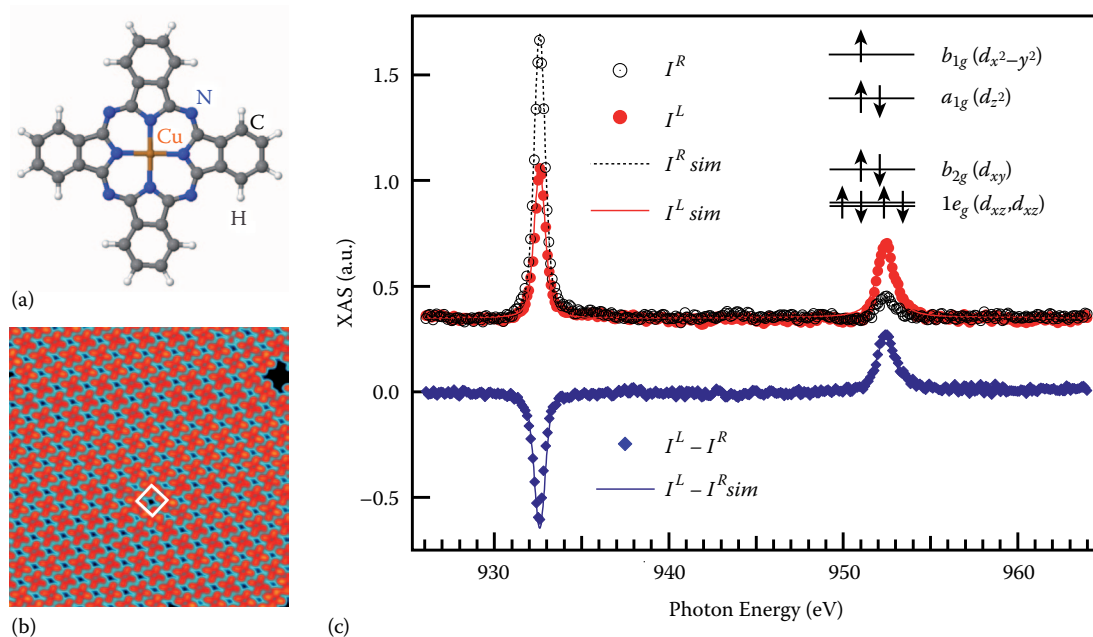
FIGURE 23.13 (a) Ball and stick model of CuPc. (b) STM image of one monolayer CuPc on Ag(100), image size 170 Å² × 170 Å². The square indicates the CuPc unit cell. (c) Circularly polarized $L_{2,3}$ XAS and XMCD of one monolayer CuPc/Ag(100) recorded at normal incidence at $B = 5$ T and $T = 6$ K. Solid and dashed lines are simulated spectra using ligand field multiplet theory, which gives the energy diagram of the Cu 3d-states shown in the inset. (Adapted from Stepanow, S. et al., *Phys. Rev. B*, 82, 014405, 2010.)
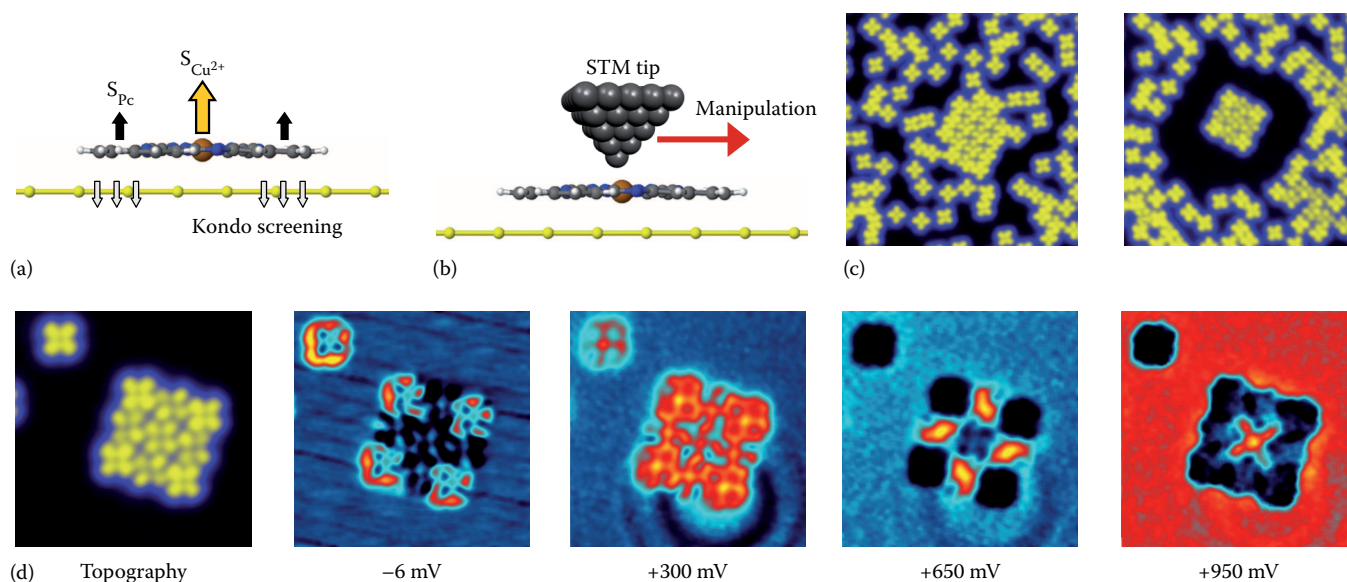

FIGURE 23.14 (See color insert.) (a) Diagram showing the spin distribution and couplings of CuPc induced by adsorption on Ag. (b) Schematic of molecule manipulation using the tip of an STM. (c) STM images showing the fabrication of a 3 × 3 CuPc cluster. (d) Topography of the cluster and spectroscopy maps (d^2I/dV^2 at −6 meV and dI/dV for the remaining maps) recorded at different energy at $T = 4.8$ K. Note that the Kondo resonance at −6 meV can be observed only for molecules with the number of lateral bonds smaller than three. The maps also show the correlation between molecular coordination, energy shift of the lowest unoccupied molecular orbital, which is responsible for the disappearance of the ligand spin. (Adapted from Mugarza, A. et al., *Nat. Commun.*, 2, 490, 2011.)

to +0.95 eV in the fourfold coordinated CuPc at the center of the cluster. The CuPc spin changes accordingly, from $S = 1$ to 1/2 [7].

Thus, the interaction between molecules and metal substrates brings about substantial changes to the molecular electronic structure and, with it, to the magnetic moment and electrical conductance. As demonstrated here, such changes are not only due to the symmetry-allowed matching of substrate and molecular orbitals but also to charge transfer effects. Lateral interactions between molecules may play a role analogous to that of an electrostatic gate, inducing strong shifts of

the molecular orbitals with respect to the Fermi level of the substrate. The magnetic moment as well as the spatial extension of the spin density in a small molecular cluster can depend on the molecule position.

23.5.3 Single Molecule Magnets on Surfaces

The molecular systems discussed earlier are essentially paramagnets. Although some molecules present large MCA, this is not sufficient to induce the blocking of the magnetic moment at reasonable temperatures. Some molecular species, however, usually including multiple transition-metal sites or rare-earth ions, present MCA energy barriers so large that their relaxation time (Equation 23.5) increases so much at low temperature that they behave similar to a ferromagnet [94]. For this reason, they are called SMMs and represent ideal candidates for both magnetic storage and quantum computing applications [95,96]. Examples are the archetypal Mn_{12} compound [94] and mononuclear Tb double-decker complexes ($TbPc_2$) [97], whose relaxation time becomes slow, compared to the time scale of observations, below a few degrees K. Measurements of $TbPc_2$, for example, show that magnetic hysteresis is measured at $T \leq 2$ K, but not above [87,98,99]. Increasing the magnetic stability independently of temperature is thus one of the greatest challenges faced by SMMs.

A useful approach to stabilize the magnetic moment of paramagnetic molecules against thermal fluctuations is that of depositing them on FM substrates. This has been demonstrated in the case of metal porphyrins and phthalocyanines using both XMCD and SP-STM [86,100–102]. However, because of the close proximity of the metal ions to the substrate, the magnetic moment of these molecules couples rigidly to the substrate magnetization, making it impossible to control their magnetic state independently from the substrate. SMMs such as $TbPc_2$, however, appear to behave in a different way [6].

Figure 23.15 shows a schematic of $TbPc_2$ deposited on FM Ni films with either out-of-plane (a) or in-plane (b) MCA. XMCD measurements allow one to probe the magnetization of Tb separately from Ni. If the easy magnetization axis of $TbPc_2$, which is out-of-plane, coincides with that of the Ni film, the magnetic moment of the molecule is effectively stabilized by the interaction with the substrate, resulting in a square magnetization hysteresis curve with nearly saturated magnetic remanence at zero applied field (Figure 23.15a). Finite magnetic remanence persists up to 100 K, a temperature that is two orders of magnitude higher compared to isolated $TbPc_2$ [6]. Depending on the strength of the applied magnetic field, we observe that both antiparallel and parallel magnetic configurations can be reached, as the Zeeman interaction compensates and eventually overcomes the exchange coupling between Tb and Ni. Moreover, if the easy
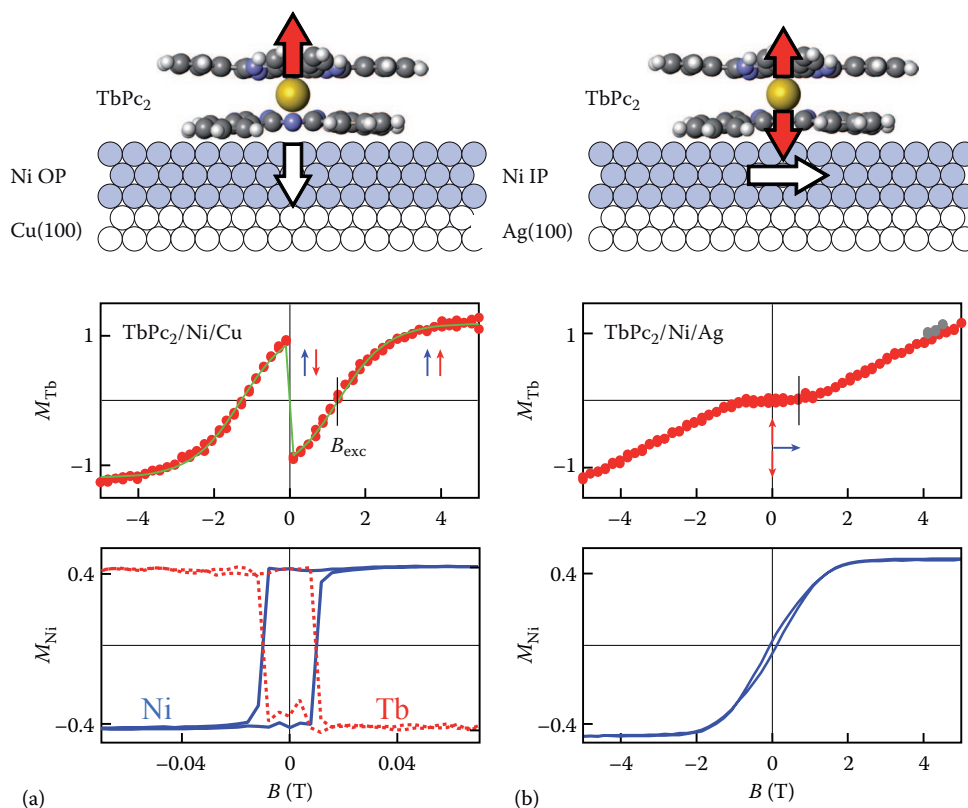

FIGURE 23.15 $TbPc_2$ single molecule magnets coupled to ferromagnetic Ni films with (a) out-of-plane and (b) in-plane easy magnetization axis. The plots show element-resolved out-of-plane magnetization loops of Ni (blue) and Tb (red) obtained by XMCD. The arrows indicate the relative orientation of the molecule and substrate magnetic moments. (Adapted from Lodi-Rizzini, A. et al., *Phys. Rev. Lett.*, 107, 177205, 2011.)

magnetization axis of the Ni film is orthogonal to that of $TbPc_2$, pronounced frustration effects are observed as the molecule magnetization cannot align with the substrate at equilibrium, and exhibits zero remanence at zero field (Figure 23.15b). Given that Tb and Ni are physically separated by a Pc ligand, an indirect exchange mechanism mediated by electrons hopping back and forth between the Pc macrocycle and Tb on one side and Ni on the other (Tb-Pc-Ni superexchange) may be responsible for the magnetic coupling. The strength of this coupling, which is in the meV range, can be tuned by electron or hole doping of the molecule–substrate interface, which is expected to change the occupation of the Pc electron orbitals [6]. This behavior also shows how the interface chemistry and magnetic response are intimately related in such systems.

In principle, SMMs can be used to store one bit of information in an extremely small volume or act as molecular-scale spin filters and injectors. The results reported earlier demonstrate enhanced thermal stability of the $TbPc_2$ magnetic moment and the possibility to orient it parallel or antiparallel to a macroscopic FM layer. Thus SMMs behave as coupled but separate magnetic units from an underlying FM substrate, which is a prerequisite for exploiting their spin as a state variable in future devices.

Acknowledgments

References

1. H. Brune and P. Gambardella, Magnetism of individual atoms adsorbed on surfaces, *Surf. Sci.* 603 (2009) 1812.

2. P. Gambardella, S. Rusponi, M. Veronese, S. S. Dhesi, C. Grazioli, A. Dallmeyer, I. Cabria et al., Giant magnetic anisotropy of single Co atoms and nanoparticles on Pt, *Science* 300 (2003) 1130.

3. P. Gambardella, S. S. Dhesi, S. Gardonio, C. Grazioli, P. Ohresser, and C. Carbone, Localized magnetic states of Fe, Co, and Ni impurities on alkali metal films, *Phys. Rev. Lett.* 88 (2002) 047202.

4. P. Gambardella, A. Dallmeyer, K. Maiti, M. C. Malagoli, S. Rusponi, P. Ohresser, W. Eberhardt, C. Carbone, and K. Kern, Oscillatory magnetic anisotropy in one-dimensional atomic wires, *Phys. Rev. Lett.* 93 (2004) 077203.

5. A. J. Heinrich, J. A. Gupta, C. P. Lutz, and D. M. Eigler, Single-atom spin-flip spectroscopy, *Science* 306 (2004) 466–469.

6. A. Lodi-Rizzini, C. Krull, T. Balashov, J. J. Kavich, A. Mugarza, P. S. Miedema, P. K. Thakur, V. Sessi, S. Klyatskaya, M. Ruben, S. Stepanow, and P. Gambardella, Coupling single molecule magnets to ferromagnetic substrates, *Phys. Rev. Lett.* 107 (2011) 177205.

7. A. Mugarza, C. Krull, R. Robles, S. Stepanow, G. Ceballos, and P. Gambardella, Spin coupling and relaxation inside molecule? metal contacts, *Nat. Commun.* 2 (2011) 490.

8. L. Zhou, J. Wiebe, S. Lounis, E. Vedmedenko, F. Meier, S. Blügel, P. H. Dederichs, and R. Wiesendanger, Strength and directionality of surface RKKY-interaction mapped on the atomic scale, *Nat. Phys.* 6 (2010) 187.

9. W. Wernsdorfer, Classical and quantum magnetization reversal studied in nanometer-sized particles and clusters, *Adv. Chem. Phys.* 118 (2001) 99.

10. W. Wernsdorfer, Quantum dynamics in molecular nanomagnets, *C. R. Chimie* 11 (2008) 1086.

11. J. S. Miller and D. Gatteschi, Molecule-based magnets, *Chem. Soc. Rev.* 40 (2011) 3065.

12. A. A. Khajetoorians, J. Wiebe, B. Chilian, and R. Wiesendanger, Realizing all-spin-based logic operations atom by atom, *Science* 332 (2011) 1062.

13. C. Carbone, S. Gardonio, P. Moras, S. Lounis, M. Heide, G. Bihlmayer, N. Atodiresei et al., Self-assembled nanometer-scale magnetic networks on surfaces: Fundamental interactions and functional properties, *Adv. Funct. Mater.* 21 (2011) 1212.

14. P. Gambardella, S. Rusponi, T. Cren, N. Weiss, and H. Brune, Magnetic anisotropy from single atoms to large monodomain islands of Co/Pt(111), *C. R. Phys.* 6 (2005) 75–87.

15. M. Bode, M. Heide, K. v. Bergmann, P. Ferriani, S. Heinze, G. Bihlmayer, A. Kubetzka, O. Pietzsch, S. Blügel, and R. Wiesendanger, Chiral magnetic order at surfaces driven by inversion asymmetry, *Nature* 447 (2007) 190.

16. M. A. Ruderman and C. Kittel, Indirect exchange coupling of nuclear magnetic moments by conduction electrons, *Phys. Rev.* 96 (1954) 99.

17. T. Kasuya, A theory of metallic ferro-and antiferromagnetism on Zener's model, *Prog. Theor. Phys.* 16 (1956) 45.

18. K. Yosida, Magnetic properties of Cu-Mn alloys, *Phys. Rev.* 106 (1957) 893.

19. A. Vindigni, A. Rettori, M. G. Pini, C. Carbone, and P. Gambardella, Finite-sized Heisenberg chains and magnetism of one-dimensional metal systems, *Appl. Phys. A* 82 (2006) 385.

20. J. Stöhr and H. C. Siegmann, *Magnetism—From Fundamentals to Nanoscale Dynamics*, Vol. 152, Springer, Berlin, Germany, 2006.

21. R. Wiesendanger, Spin mapping at the nanoscale and atomic scale, *Rev. Mod. Phys.* 81 (2009) 1495.

22. B. T. Thole, G. v. d. Laan, J. C. Fuggle, G. A. Sawatzky, R. C. Karnatak, and J. M. Esteva, 3d x-ray-absorption lines and the 3d94fn+1 multiplets of the lanthanides, *Phys. Rev. B* 32 (1985) 5107.

23. G. v. d. Laan and B. T. Thole, Strong magnetic x-ray dichroism in 2p absorption spectra of 3d transition-metal ions, *Phys. Rev. B* 43 (1991) 13401–13411.

24. B. T. Thole, P. Carra, F. Sette, and G. v. d. Laan, X-ray circular dichroism as a probe of orbital magnetization, *Phys. Rev. Lett*. 68 (1992) 1943–1946.

25. P. Carra, B. T. Thole, M. Altarelli, and X. Wang, X-ray circular dichroism and local magnetic fields, *Phys. Rev. Lett*. 70 (1993) 694–697.

26. C. T. Chen, Y. U. Idzerda, H. J. Lin, N. V. Smith, G. Meigs, E. Chaban, G. H. Ho, E. Pellegrin and F. Sette, Experimental confirmation of the X-ray magnetic circular dichroism sum rules for iron and cobalt, *Phys. Rev. Lett*. 75 (1995) 152–155.

27. S. Stepanow, A. Mugarza, G. Ceballos, P. Moras, J. Cezar, C. Carbone, and P. Gambardella, Giant spin and orbital moment anisotropies of a Cu-phthalocyanine monolayer, *Phys. Rev. B* 82 (2010) 014405.

28. A. Yazdani, B. A. Jones, C. P. Lutz, M. F. Crommie, and D. M. Eigler, Probing the local effects of magnetic impurities on superconductivity, *Science* 275 (1997) 1767–1770.

29. E. W. Hudson, K. M. Lang, V. Madhavan, S. H. Pan, H. Eisaki, S. Uchida, and J. C. Davis, Interplay of magnetism and high-Tc superconductivity at individual Ni impurity atoms in $Bi_2Sr_2CaCu_2O_8$+delta, *Nature* 411 (2001) 920–924.

30. L. Bürgi, *Scanning Tunneling Microscopy as Local Probe of Electron Density, Dynamics, and Transport at Metal Surfaces*, Ph.D. thesis, Swiss Federal Institute of Technology, Lausanne, Switzerland, (1999).

31. J. Li, W. D. Schneider, R. Berndt, and B. Delley, Kondo scattering observed at a single magnetic impurity, *Phys. Rev. Lett*. 80 (1998) 2893.

32. M. Ternes, A. J. Heinrich, and W. D. Schneider, Spectroscopic manifestations of the Kondo effect on single adatoms, *J. Phys.: Condens. Matter* 21 (2009) 053001.

33. V. Madhavan, W. Chen, T. Jamneala, M. F. Crommie, and N. S. Wingreen, Tunneling into a single magnetic atom: Spectroscopic evidence of the kondo resonance, *Science* 280 (1998) 567–569.

34. J. Kröger, N. Néel, and L. Limot, Contact to single atoms and molecules with the tip of a scanning tunnelling microscope, *J. Phys.: Condens. Matter* 20 (2008) 223001.

35. R. Wiesendanger, H. J. Güntherodt, G. Güntherodt, R. J. Gambino, and R. Ruf, Observation of vaccum tunneling of spin-polarized electrons with the scanning tunneling microscope, *Phys. Rev. Lett*. 65 (1990) 247.

36. M. Bode, Spin-polarized scanning tunnelling microscopy, *Rep. Prog. Phys*. 66 (2003) 523.

37. W. Wulfhekel and J. Kirschner, Spin-polarized scanning tunneling microscopy of magnetic structures and antiferromagnetic thin films, *Ann. Rev. Mater. Res*. 37 (2007) 69.

38. S. Krause, L. Berbil-Bautista, G. Herzog, M. Bode, and R. Wiesendanger, Current-induced magnetization switching with a spin-polarized scanning tunneling microscope, *Science* 317 (2007) 1537.

39. S. Rusponi, N. Weiss, T. Cren, M. Epple, and H. Brune, High tunnel magnetoresistance in spin-polarized scanning tunneling microscopy of Co nanoparticles on Pt(111), *Appl. Phys. Lett*. 87 (2005) 162514.

40. W. A. Hofer, K. Palotás, S. Rusponi, T. Cren, and H. Brune, Role of hydrogen in giant spin polarization observed on magnetic nanostructures, *Phys. Rev. Lett*. 100 (2008) 026806.

41. F. Meier, L. Zhou, J. Wiebe, and R. Wiesendanger, Revealing magnetic interactions from single-atom magnetization curves, *Science* 320 (2008) 82–86.

42. G. Rodary, S. Wedekimd, D. Sander, and J. Kirschner, Magnetic hysteresis loop of single co nano-islands, *Jpn. J. Appl. Phys*. 47 (2008) 9013.

43. A. A. Khajetoorians, J. Wiebe, B. Chilian, S. Lounis, S. Blügel, and R. Wiesendanger, Atom-by-atom engineering and magnetometry of tailored nanomagnets, *Nat. Phys*. 8 (2012) 497.

44. H. Oka, K. Tao, S. Wedekind, G. Rodary, V. Stepanyuk, D. Sander, and J. Kirschner, Spatially modulated tunnel magnetoresistance on the nanoscale, *Phys. Rev. Lett*. 107 (2011) 187201.

45. S. Ouazi, S. Wedekind, G. Rodary, H. Oka, D. Sander, and J. Kirschner, Magnetization reversal of individual co nanoislands, *Phys. Rev. Lett*. 108 (2012) 107206.

46. C. F. Hirjibehedin, C. P. Lutz, and A. J. Heinrich, Spin-coupling in engineered atomic structures, *Science* 312 (2006) 1021.

47. C. F. Hirjibehedin, C. Y. Lin, A. F. Otte, M. Ternes, C. P. Lutz, B. A. Jones, and A. J. Heinrich, Large magnetic anisotropy of a single atomic spin embedded in a surface molecular network, *Science* 317 (2007) 1199–1203.

48. A. F. Otte, M. Ternes, K. v. Bergmann, S. Loth, H. Brune, C. P. Lutz, C. F. Hirjibehedin, and A. J. Heinrich, The role of magnetic anisotropy in the Kondo effect, *Nat. Phys*. 4 (2008) 847.

49. T. Balashov, T. Schuh, A. F. Takács, A. Ernst, S. Ostanin, J. Henk, I. Mertig, P. Bruno, T. Miyamachi, S. Suga, and W. Wulfhekel, Magnetic anisotropy and magnetization dynamics of individual atoms and clusters of Fe and Co on Pt(111), *Phys. Rev. Lett*. 102 (2009) 257203.

50. A. A. Khajetoorians, B. Chilian, J. Wiebe, S. Schuwalow, F. Lechermann, and R. Wiesendanger, Detecting excitation and magnetization of individual dopants in a semiconductor, *Nature* 467 (2010) 1084.

51. A. A. Khajetoorians, S. Lounis, B. Chilian, A. T. Costa, L. Zhou, D. L. Mills, J. Wiebe, and R. Wiesendanger, Itinerant nature of atom-magnetization excitation by tunneling electrons, *Phys. Rev. Lett*. 106 (2011) 037205.

52. J. Lambe, R. C. Jaklevic, Molecular vibration spectra by inelastic electron tunneling, *Phys. Rev*. 165 (1968) 821.

53. E. L. Wolf, *Principles of Electron Tunneling Spectroscopy*, Oxford University Press, New York, 1989.

54. B. C. Stipe, M. A. Rezaei, and W. Ho, Single molecule vibrational spectroscopy and microscopy, *Science* 280 (1998) 1732.

55. T. Balashov, A. F. Takacs, W. Wulfhekel, and J. Kirschner, Magnon excitation with spin-polarized Scanning Tunneling Microscopy, *Phys. Rev. Lett.* 97 (2006) 187201.

56. S. Loth, S. Baumann, C. P. Lutz, D. M. Eigler, and A. J. Heinrich, Bistability in atomic-scale antiferromagnets, *Science* 335 (2012) 196.

57. S. Loth, K. v. Bergmann, C. P. Lutz, and A. J. Heinrich, Spin-polarized spin excitation spectroscopy, *N. J. Phys.* 12 (2010) 125021.

58. S. Loth, K. v. Bergmann, M. Ternes, A. F. Otte, C. P. Lutz, and A. J. Heinrich, Controlling the state of quantum spins with electric currents, *Nat. Phys.* 6 (2010) 340.

59. S. Loth, M. Etzkorn, C. P. Lutz, D. M. Eigler, and A. J. Heinrich, Measurement of fast electron spin relaxation times with atomic resolution, *Science* 329 (2010) 1628.

60. C. Carbone, M. Veronese, P. Moras, S. Gardonio, C. Grazioli, P. H. Zhou, O. Rader et al., Correlated electrons step by step: Itinerant-to-localized transition of Fe impurities in free-electron metal hosts, *Phys. Rev. Lett.* 104 (2010) 117601.

61. P. W. Anderson, Localized magnetic states in metals, *Phys. Rev.* 124 (1961) 41.

62. H. Brune, Microscopic view of epitaxial metal growth: nucleation and aggregation, *Surf. Sci. Rep.* 31 (1998) 121.

63. S. Blügel, Two-dimensional ferromagnetism of 3d, 4d, and 5d transition metal monolayers on noble metal (001) substrates, *Phys. Rev. Lett.* 68 (1992) 851.

64. P. Lang, V. S. Stepanyuk, K. Wildberger, R. Zeller, and P. H. Dederichs, Local moments of 3d, 4d, and 5d atoms at Cu and Ag(001) surfaces, *Solid State Commun.* 92 (1994) 755.

65. B. Nonas, I. Cabria, R. Zeller, P. H. Dederichs, T. Huhne, and H. Ebert, Strongly enhanced orbital moments and anisotropies of adatoms on the Ag(100) surface, *Phys. Rev. Lett.* 86 (2001) 2146.

66. S. Blügel, Magnetism goes nano: 36th IFF Spring School, In: S. Blügel, T. Brückel, C. M. Schneider eds., Ch. *Reduced Dimensions I: Magnetic Moment and Magnetic Structure*, Forschungszentrums Jülich, Jülich, 2005.

67. G. J. Nieuwenhuys, Magnetic behaviour of cobalt, iron and manganese dissolved in palladium, *Adv. Phys.* 24 (1975) 515.

68. Y. Yayon, X. H. Lu, and M. F. Crommie, Bimodal electronic structure of isolated Co atoms on Pt(111), *Phys. Rev. B* 73 (2006) 155401.

69. G. Kresse, M. Schmid, E. Napetschnig, M. Shishkin, L. Köhler, and P. Varga, Structure of the ultrathin aluminum oxide film on NiAl (110), *Science* 308 (2005) 1440.

70. H. Ellmer, V. Repain, M. Sotto, and S. Rousset, Pre-structured metallic template for the growth of ordered, square-based nanodots, *Surf. Sci.* 511 (2002) 183.

71. B. Croset, Y. Girard, G. Prévot, M. Sotto, Y. Garreau, R. Pinchaux, and M. Sauvage-Simkin, Measuring surface stress discontinuities in self-organized systems with X rays, *Phys. Rev. Lett.* 88 (2002) 56103.

72. T. Choi, C. D. Ruggiero, and J. A. Gupta, Incommensurability and atomic structure of c(2×2)N/Cu(100): A scanning tunneling microscopy study, *Phys. Rev. B* 78 (2008) 035430.

73. D. M. Eigler, C. P. Lutz, and W. E. Rudge, An atomic switch realized with the scanning tunneling microscope, *Nature* 352 (1991) 600–603.

74. L. Bartels, G. Meyer, and K. H. Rieder, Basic steps of lateral manipulation of single atoms and diatomic clusters with a scanning tunneling microscope, *Phys. Rev. Lett.* 79 (1997) 697–700.

75. H. Brune, Assembly and probing of spin chains of finite size, *Science* 312 (2006) 1005.

76. N. Tsukahara, K. I. Noto, M. Ohara, S. Shiraki, N. Takagi, Y. Takata, J. Miyawaki, M. Taguchi, A. Chainani, S. Shin, and M. Kawai, Adsorption-induced switching of magnetic anisotropy in a single iron(II) phthalocyanine molecule on an oxidized Cu(110) surface, *Phys. Rev. Lett.* 102 (2009) 167203.

77. A. Mugarza and P. Gambardella, Orbital specific chirality and homochiral self-assembly of achiral molecules induced by charge transfer and spontaneous symmetry breaking, *Phys. Rev. Lett.* 105 (2010) 115702.

78. X. Chen, Y. S. Fu, S. H. Ji, T. Zhang, P. Cheng, X. C. Ma, X. L. Zou, W. H. Duan, J. F. Jia, and Q. K. Xue, Probing superexchange interaction in molecular magnets by spin-flip spectroscopy and microscopy, *Phys. Rev. Lett.* 101 (2008) 197208.

79. K. Tao, V. S. Stepanyuk, W. Hergert, I. Rungger, S. Sanvito, and P. Bruno, Switching a single spin on metal surfaces by a STM tip: ab initio studies, *Phys. Rev. Lett.* 103 (2009) 057202.

80. F. Delgado, J. J. Palacios, and J. Fernandez-Rossier, Spin-transfer torque on a single magnetic adatom, *Phys. Rev. Lett.* 104 (2010) 026601.

81. M. Bode, O. Pietzsch, A. Kubetzka, and R. Wiesendanger, Shape-dependent thermal switching behavior of superpara-magnetic nanoislands, *Phys. Rev. Lett.* 92 (2004) 067201.

82. S. Krause, G. Herzog, T. Stapelfeldt, L. Berbil-Bautista, M. Bode, E. Y. Vedmedenko, and R. Wiesendanger, Magnetization reversal of nanoscale islands: How size and shape affect the arrhenius prefactor, *Phys. Rev. Lett.* 103 (2009) 127202.

83. S. Rusponi, T. Cren, N. Weiss, M. Epple, P. Buluschek, L. Claude, and H. Brune, The remarkable difference between surface and step atoms in the magnetic anisotropy of 2D nanostructures, *Nat. Mater.* 2 (2003) 546.

84. P. Gambardella, A. Dallmeyer, K. Maiti, M. C. Malagoli, W. Eberhardt, K. Kern, and C. Carbone, Ferromagnetism in one-dimensional monatomic metal chains, *Nature* 416 (2002) 301–304.

85. P. Gambardella, S. Stepanow, A. Dmitriev, J. Honolka, F. M. F. d. Groot, M. Lingenfelder, S. S. Gupta et al., Supramolecular control of the magnetic anisotropy in two-dimensional high-spin Fe arrays at a metal interface, *Nat. Mater.* 8 (2009) 189.

86. M. Bernien, J. Miguel, C. Weis, M. E. Ali, J. Kurde, B. Krumme, P. M. Panchmatia et al., Tailoring the nature of magnetic coupling of Fe-porphyrin molecules to ferromagnetic substrates, *Phys. Rev. Lett.* 102 (2009) 047202.

87. S. Stepanow, J. Honolka, P. Gambardella, L. Vitali, N. Abdurakhmanova, T. C. Tseng, S. Rauschenbach et al., Spin and orbital magnetic moment anisotropies of monodispersed bis(phthalocyaninato) terbium on a copper surface, *J. Am. Chem. Soc.* 132 (2010) 11900.

88. A. Mugarza, R. Robles, C. Krull, R. Korytr, N. Lorente, and P. Gambardella, Electronic and magnetic properties of molecule-metal interfaces: Transition-metal phthalocyanines adsorbed on Ag(100), *Phys. Rev. B* 85 (2012) 155437.

89. S. Stepanow, P. S. Miedema, A. Mugarza, G. Ceballos, P. Moras, J. C. Cezar, C. Carbone, F. M. F. d. Groot, and P. Gambardella, Mixed-valence behavior and strong correlation effects of metal phthalocyanines adsorbed on metals, *Phys. Rev. B* 83 (2011) 220401.

90. M. A. Lingenfelder, H. Spillmann, A. Dmitriev, S. Stepanow, N. Lin, J. V. Barth, and K. Kern, Towards surface-supported supramolecular architectures: Tailored coordination assembly of 1,4-Benzenedicarboxylate and Fe on Cu(100), *Chem. Eur. J* 10 (2004) 1913.

91. S. Stepanow, N. Lin, and J. V. Barth, Modular assembly of low-dimensional coordination architectures on metal surfaces, *J. Phys.: Condens. Matter* 20 (2008) 184002.

92. L. Gao, W. Ji, Y. B. Hu, Z. H. Cheng, Z. T. Deng, Q. Liu, N. Jiang et al., Site-specific kondo effect at ambient temperatures in iron-based molecules, *Phys. Rev. Lett.* 99 (2007) 106402.

93. J. Brede, N. Atodiresei, S. Kuck, P. Lazic, V. Caciuc, Y. Morikawa, G. Hoffmann, S. Blügel, and R. Wiesendanger, Spin- and energy-dependent tunneling through a single molecule with intramolecular spatial resolution, *Phys. Rev. Lett.* 105 (2010) 047204.

94. R. Sessoli, D. Gatteschi, A. Caneschi, and M. A. Novak, Magnetic bistability in a metal-ion-cluster, *Nature* 365 (1993) 141.

95. L. Bogani and W. Wernsdorfer, Molecular spintronics using single-molecule magnets, *Nat. Mater.* 7 (2008) 179.

96. M. N. Leuenberger and D. Loss, Quantum computing in molecular magnets, *Nature* 410 (2001) 789.

97. N. Ishikawa, M. Sugita, T. Ishikawa, S. Koshihara, and Y. Kaizu, Lanthanide double-decker complexes functioning as magnets at the single-molecular level, *J. Am. Chem. Soc.* 125 (2003) 8694.

98. L. Margheriti, D. Chiappe, M. Mannini, P. Car, P. Sainctavit, M. A. Arrio, F. B. d. Mongeot et al., X-ray detected magnetic hysteresis of thermally evaporated terbium double-decker oriented films, *Adv. Mater.* 22 (2010) 5488.

99. R. Biagi, J. Fernandez-Rodriguez, M. Gonidec, A. Mirone, V. Corradini, F. Moro, V. De Renzi, U. del Pennino, J. C. Cezar, D. B. Amabilino, and J. Veciana, X-ray absorption and magnetic circular dichroism investigation of bis(phthalocyaninato) terbium single-molecule magnets deposited on graphite, *Phys. Rev. B* 82 (2010) 224406.

100. A. Scheybal, T. Ramsvik, R. Bertschinger, M. Putero, F. Nolting, and T. A. Jung, Induced magnetic ordering in a molecular monolayer, *Chem. Phys. Lett.* 411 (2005) 214.

101. C. Iacovita, M. V. Rastei, B. W. Heinrich, T. Brumme, J. Kortus, L. Limot, and J. P. Bucher, Visualizing the spin of individual cobalt-phthalocyanine molecules, *Phys. Rev. Lett.* 101 (2008) 116602.

102. S. Javaid, M. Bowen, S. Boukari, L. Joly, J. B. Beaufrand, X. Chen, Y. J. Dappe et al., Impact on interface spin polarization of molecular bonding to metallic surfaces, *Phys. Rev. Lett.* 105 (2010) 077201.